Emerging applications of carbon nanohoops

Erik J. Leonhardt and Ramesh Jasti *

Abstract | A cycloparaphenylene can be thought of as the shortest possible cross section of an armchair carbon nanotube. Although envisioned decades ago, these molecules — also referred to as carbon nanohoops — can be highly strained and, thus, eluded chemical synthesis. However, the past decade has seen the development of methods to access carbon nanohoops of varying size and composition. In contrast to many carbon-rich materials, the nanohoops are atom-precise and structurally tunable because they are prepared by stepwise organic synthesis. Accordingly, a variety of unique, size-dependent optoelectronic and host–guest properties have been uncovered. In this Review, we highlight recent research that aims to leverage the unique physical properties of nanohoops in applications and emphasize the connection between structure and properties.

The pursuit of unusual and synthetically challenging molecular entities often results in unpredictable developments in terms of applications. This is perhaps unsurprising, given that unique molecular architectures often give rise to novel chemical properties. Possessing strikingly distorted phenylene moieties and radially oriented π-systems, the cycloparaphenylenes (CPPs) — often referred to as carbon nanohoops — exemplify how a unique molecular form can afford equally unique functions[1] (BOX 1). Initially envisioned as seeds from which to begin the size-selective growth of carbon nanotubes (CNTs), CPPs have, since their first synthesis in 2008 by Jasti, Bertozzi and colleagues, quickly established themselves as interesting molecules in their own right. This is in no small part due to the bent cyclic geometries of CPPs exhibiting a wealth of unexpected, unique photophysical and electronic properties[2–7]. In parallel with these studies, our synthetic methodologies have advanced to allow access to CPPs on the gram scale[8–10] — a roughly three-orders-of-magnitude increase over the first synthesis[1]. Likewise, a variety of synthetic strategies have been developed that allow bottom-up functionalization of CPPs to further fine-tune their properties[11–17]. With ready access to tunable CPPs, many chemists have sought to explore their practical utility.

In this Review, we focus primarily on the applications of CPPs that have begun to surface in the literature throughout the past 5 years. These applications include the implementation of CPPs as novel solution-state and solid-state fluorophores[18–21], organic electronic components[10,22,23] and synthons for the construction of bulk supramolecular, carbon-rich nanomaterials[24–26]. We also describe how these properties are intimately connected to the strained, cyclic nature of the nanohoop structures. The development of CPP syntheses has been covered thoroughly in numerous reviews[27–31] and we thus choose not to focus on synthetic developments; a brief summary of general synthetic approaches towards CPPs can be found in BOX 1. Likewise, non-applied synthetic landmarks in the field of nanohoop chemistry will not be covered, although we acknowledge recent advancements in the syntheses of both aromatic belts and interlocked CPP-based structures[32–34]. We speculate here on potential CPP applications, proposing CPPs as potential imaging agents for the study of complex biological phenomena, electronic materials that are tunable by functionalization or guest uptake and building blocks for atomically precise CNT mimics.

CPPs as versatile fluorophores

The structures of [*n*]CPPs (where *n* is the number of phenylene units in the hoop) are strained and non-planar, and afford size-dependent photophysical phenomena[2–7]. Specifically, the energy gap between the highest occupied molecular orbital (HOMO) and the lowest unoccupied molecular orbital (LUMO) of a CPP decreases with decreasing numbers of phenylenes in the hoop (FIG. 1a). This trend is opposite to that observed for linear oligo(*para*-phenylene) species, the HOMO–LUMO gaps of which decrease with increasing *n* due to extended conjugation[35]. Although decreasing the number of phenylene moieties in a [*n*]CPP lowers the potential extent of conjugation, it also leads to radial planarity of the π-system (a lowering of torsional angles) due to increased strain (FIG. 1b,c). The average dihedral angle θ between phenylenes in odd-numbered CPPs is typically

Department of Chemistry and Biochemistry, Materials Science Institute, Knight Campus for Accelerating Scientific Impact, University of Oregon, Eugene, OR, USA.

**e-mail: rjasti@uoregon.edu*

https://doi.org/10.1038/s41570-019-0140-0

Box 1 | **Cycloparaphenylenes are the smallest cross-sectional fragments of armchair carbon nanotubes**

A cycloparaphenylene [*n*]CPP consists of *n* *para*-phenylene moieties linked together to form a hoop[1]. [5]CPP resembles the armchair edge of the carbon nanotube [5,5]CNT (see the figure, part **a**). [*n*]CPPs feature a strained structure with a radially oriented π-electron system and an electron-rich central cavity similar to that in carbon nanotubes[139] (see the figure, part **b**). Three common synthetic routes to cycloparaphenylenes are shown (see the figure, part **c**). Two routes make use of cyclohexadiene[1] and cyclohexane[99] as 'masked' benzene rings. These sp^3-C-containing precursors have the appropriate curvature and are subjected to a strain-building aromatization step to afford the desired cycloparaphenylene ([12]CPP in this case). An alternative route employs a Pt molecular square with 4,4′-biphenylene sides, reductive elimination of which affords a [4*n*]CPP, such as [8]CPP[99].

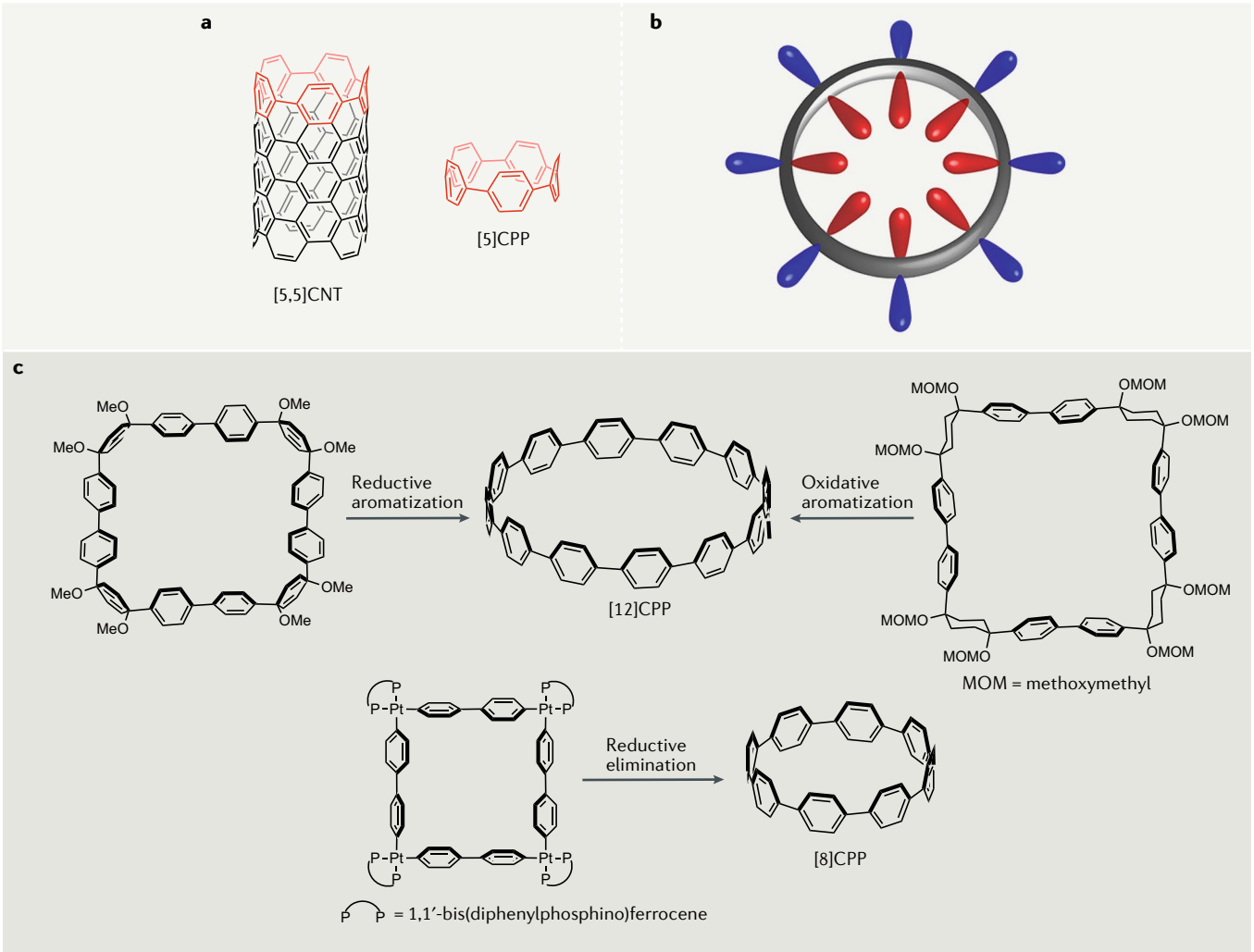

lower than the trend would imply due to greater angular variance[36,37]. Despite the different energies of their frontier molecular orbitals, all CPPs share a common absorbance maximum at ~340 nm (FIG. 1b,c) assigned to a symmetry-forbidden (on account of centrosymmetry) HOMO→LUMO electronic transition[3]. Because of this, the absorptions observed for CPPs of all sizes are the result of energetically similar transitions, such as HOMO→LUMO+1/LUMO+2 and HOMO−1/HOMO−2→LUMO. By contrast, CPP emission red-shifts with decreasing *n* (FIG. 1b,c), which follows the HOMO–LUMO trend. A theoretical study[38] indicates that CPP emission is dependent on the breaking of orbital symmetry in the excited state, which results from partial planarization of the nanohoop backbone (FIG. 1d). Therefore, by simply changing *n*, we can access emission maxima in the range 450–587 nm (in the *n* = 7–12 series) without functionalization of the nanohoop backbone.

The strain-induced planarization that gives rise to the unique photophysical properties of CPPs also prevents emission from smaller nanohoops (*n* = 5, 6)[38–40]. Thus, the substantial strain present in [5]CPP and [6]CPP (119 kcal mol^{-1} and 97 kcal mol^{-1}, respectively)[39,40] inhibits partial planarization and the breaking of orbital symmetry in their respective excited states[38], such that fluorescence emission is Laporte-forbidden (FIG. 1d). However, the emission window accessible using nanohoop structures can be expanded by breaking molecular symmetry, as can be achieved by introducing a single *meta* connectivity[41]. For example, a series of [*n*]CPPs (*n* = 5–8, 10, 12) in which a single phenylene is *meta* substituted (denoted *m*[*n*]CPPs; FIG. 1e)

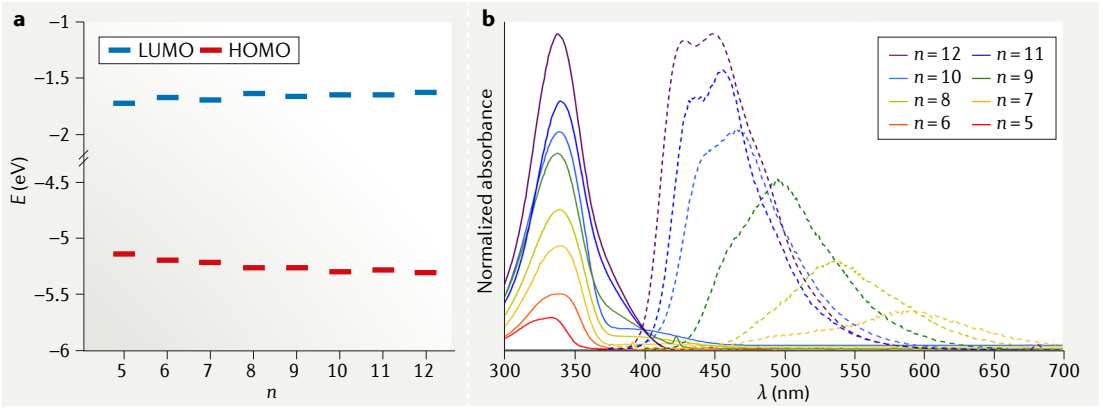

c

[*n*]CPP	λ_{max} (nm)	$\varepsilon_{\lambda_{max}}$ ($M^{-1}cm^{-1}$)	λ_{em} (nm)	θ_{approx}	$\Phi_{\lambda_{max}}$	Brightness ($\varepsilon_{\lambda_{max}} \times \Phi_{\lambda_{max}}$)
5	335	5.7×10^4	Non-emissive	16°	0	0
6	340	–	Non-emissive	28°	0	0
7	340	6.9×10^4	587	25°	0.007	4.8×10^2
8	340	1.0×10^5	533	31°	0.10	1.0×10^4
9	340	1.2×10^5	494	30°	0.38	4.6×10^4
10	338	1.3×10^5	466	32°	0.65	8.5×10^4
11	340	1.3×10^5	458	32°	0.73	9.5×10^4
12	339	1.4×10^5	450	34°	0.81	1.4×10^5

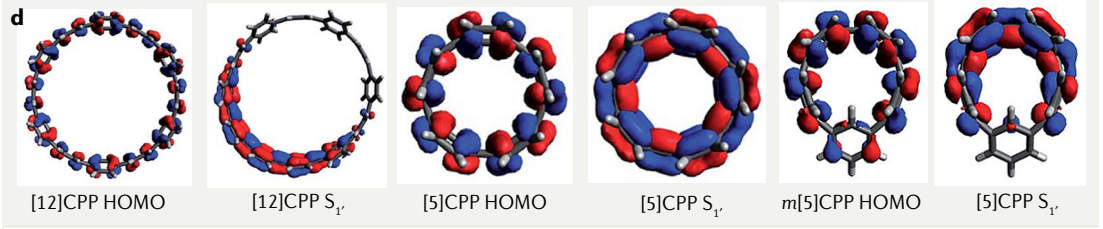

e

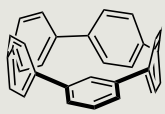

f

m[*n*]CPP	λ_{em} (nm)	Brightness ($\varepsilon_{\lambda_{max}} \times \Phi_{\lambda_{max}}$)
5	534	4.2×10^2
6	510	1.2×10^4
7	491	2.3×10^4
8	484	3.7×10^4
10	456	5.2×10^4
12	429	7.7×10^5

Fig. 1 | **The electronic structures of cycloparaphenylenes are size-dependent. a** | The energies of the highest occupied molecular orbital (HOMO) and the lowest unoccupied molecular orbital (LUMO) in a [*n*]CPP (*n* = 5–12) lead to an energy gap $E_g = E_{HOMO} - E_{LUMO}$ that decreases with decreasing *n*. **b** | Ultraviolet–visible absorption and emission spectra (solid and dashed traces, respectively) of [5–12]CPP. **c** | The photophysical properties of [5–12]CPP and average dihedral angles between phenylenes in optimized geometries[37]. **d** | Orbitals in electronic ground and excited states of [12]CPP, [5]CPP and *m*[5]CPP. **e** | Generic structure of *m*[*n*]CPP. **f** | Photophysical data for *m*[*n*]CPP (*n* = 5–8, 10, 12). Parts **a** and **b** adapted with permission from REF.[27]. Part **d** adapted with permission from REF.[41], Royal Society of Chemistry (https://doi.org/10.1039/C9SC00169G).

exhibits size-dependent emission almost identical in nature to that observed for the all-*para*-linked CPPs. The incorporation of a *meta*-linked phenylene allows for excited-state orbital symmetry breaking in each of the studied *m*[*n*]CPP species, with even *m*[5]CPP displaying moderately bright emission ($\varepsilon_{\lambda max} \times \Phi_{\lambda max} = 4.2 \times 10^2$). Importantly, the brightness of the *m*[*n*]CPPs was found to be comparable to or even greater than that of their respective all-*para*-linked counterparts[1,39,40,42–45] (FIG. 1f), thus providing a viable alternative strategy for accessing the unique, size-dependent emissive properties of CPPs. Additionally, as with CPPs, the *m*[*n*]CPPs all share a common absorbance, here at ~328 nm. As will be discussed below, both [*n*]CPPs and the more recently developed *m*[*n*]CPPs are quickly proving themselves to be effective scaffolds for fluorophore development.

CPP rotaxanes as fluorescent sensors. Interlocked architectures such as rotaxanes and catenanes[46] have garnered a great deal of attention, not least serving as the basis of the Nobel Prize in Chemistry 2016 (REF.[47]). A variety of applications of these systems are beginning to take shape[48–52], notable among which are sensors comprising interlocked systems in which the thread component exhibits a photophysical response to a particular analyte[49,50,53]. With CPPs being rare examples of highly emissive macrocycles, we were curious to investigate whether one could invert this paradigm and have the macrocycle

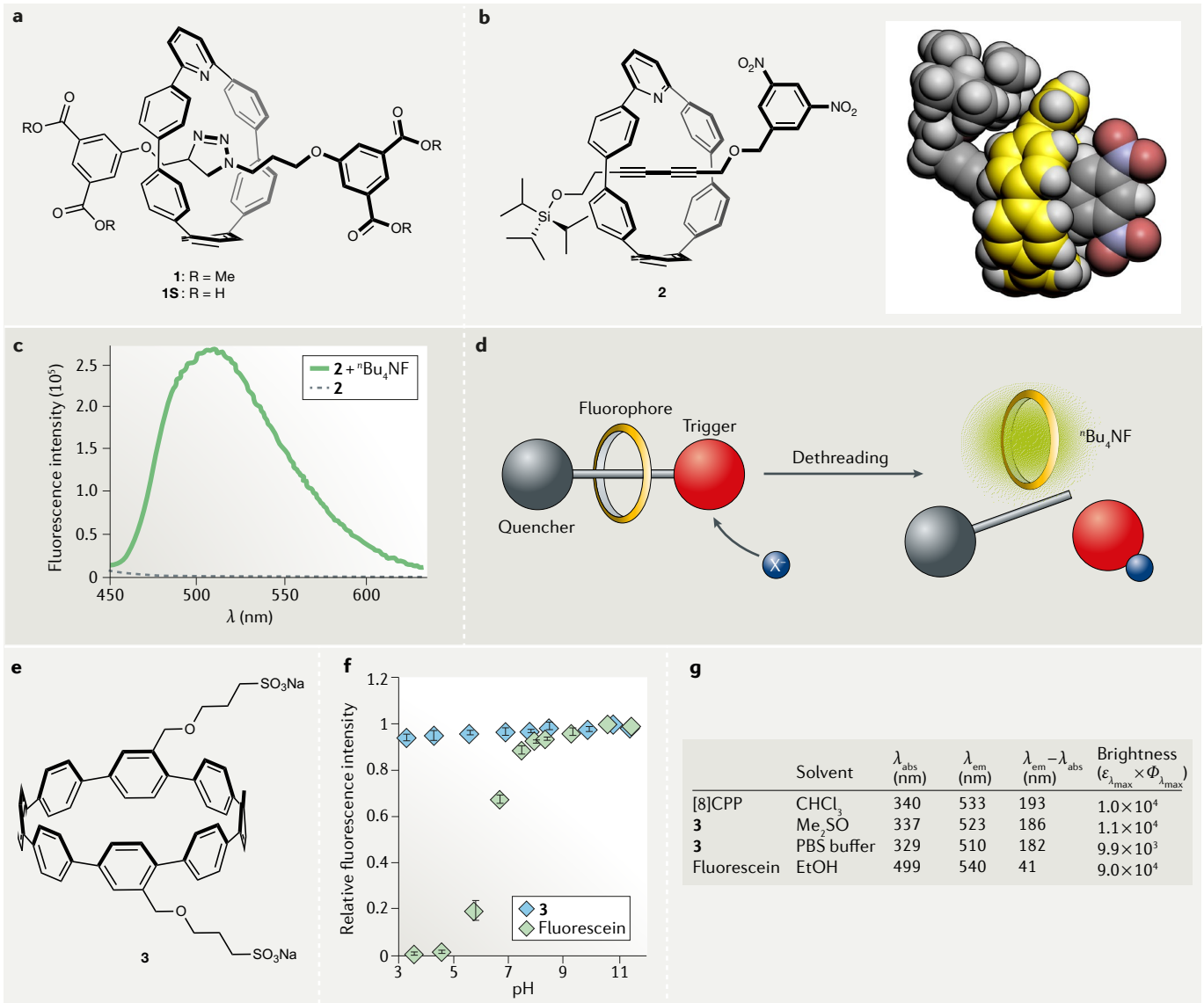

	Solvent	λ_{abs} (nm)	λ_{em} (nm)	$\lambda_{em}-\lambda_{abs}$ (nm)	Brightness ($\varepsilon_{\lambda_{max}} \times \Phi_{\lambda_{max}}$)
[8]CPP	$CHCl_3$	340	533	193	1.0×10^4
3	Me_2SO	337	523	186	1.1×10^4
3	PBS buffer	329	510	182	9.9×10^3
Fluorescein	EtOH	499	540	41	9.0×10^4

Fig. 2 | **Applications of cycloparaphenylenes in biological imaging. a** | Pyridyl-*m*[6]CPP rings can bind a catalytic Cu^{I} ion and serve as the active template in the synthesis of rotaxanes **1** and **1S**, which bear a triazole-containing thread. **b** | The pyridyl-*m*[6]CPP ring, in conjunction with Cu^{I}, can also mediate alkyne–alkyne coupling to give diyne rotaxane **2**, the X-ray crystal structure of which is also presented. **c** | Fluorescence turn-on of **2** on treatment with ^{n}Bu$_4$NF. **d** | Desilylation of **2** with F^- leads to dethreading and liberation of the emissive pyridyl-*m*[6]CPP ring. **e** | Structure of a bis(sulfonate) derivative of [8]CPP (**3**). **f** | Fluorescence emission from **3** and fluorescein is pH-dependent. **g** | Photophysical data of **3**, [8]CPP and fluorescein. Parts **b** and **c** adapted with permission from REF.[18], Wiley-VCH. Parts **f** and **g** adapted with permission from REF.[19], American Chemical Society.

serve as the responsive component of a rotaxane sensor. For example, an interlocked *m*[*n*]CPP scaffold, where the *meta*-substitution takes the form of a 2,6-substituted pyridine, has been incorporated into small-molecule sensing platforms[18] (FIG. 2a,b). A key design feature of pyridyl-*m*[*n*]CPPs is the position of the N atom — directed towards the inside of the nanohoop. This atom can bind a metal such as Cu^{I}, which can mediate an azide–alkyne cycloaddition or a Cadiot–Chodkiewicz alkyne cross-coupling within the nanohoop cavity. This approach, in which the nanohoops act as ligands to promote coupling reactions within the macrocyclic pore, is often referred to as an active template strategy[52,54,55].

The fluorescence from **1**, a pyridyl-*m*[6]CPP-based rotaxane with dimethyl isophthalate stoppers (FIG. 2a), could be almost entirely quenched by adding equimolar $[Pd(MeCN)_4](BF_4)_2$. This effect, presumably due to coordination of Pd^{II} to the triazole in the thread and the pyridyl in the nanohoop, is reversible — demetallating the complex with one molar equivalent of ethylenediaminetetraacetate resulted in a 30-fold increase in emission intensity. Hydrolysis of the ester groups in rotaxane **1** affords the H_2O-soluble carboxylic acid derivative **1S** (FIG. 2a), which exhibited the same turn-on sensor behaviour with a 10-fold increase in fluorescence upon demetallation. These responsive nanohoop rotaxanes

inspired the design of unsymmetrical rotaxanes such as **2**, which bears a pyridyl-*m*[6]CPP around a butadiyne thread with bulky Si^iPr_3 and 3,5-dinitrobenzene stopper groups on either end (FIG. 2b). Emission from the nanohoop is completely quenched when it exists as part of the rotaxane, and density functional theory calculations suggest that this is a result of charge transfer from the nanohoop to the dinitrobenzene stopper group. Adding $^nBu_4NF$ cleaves off the Si^iPr_3 stopper, leading to dethreading and a striking 123-fold increase in fluorescence intensity (FIG. 2c,d). Nanohoop-containing interlocked structures are thus predicted to afford tunable platforms from which to develop small-molecule sensors. Additionally, one can imagine that the Si^iPr_3 group of nanohoop **2** could be replaced with a variety of cleavable functional groups, allowing this scaffold to be engineered to sense a myriad of small molecules beyond F^-. Indeed, pyridyl-*m*[6]CPP is relatively small, such that its dethreading can be prevented by a wide variety of stoppers, even relatively small groups.

CPPs as biological fluorophores. Imaging techniques that rely on small-molecule fluorescent dyes are becoming increasingly important tools for studying biological phenomena at the cellular level[56–58]. Despite this, there is a surprising dearth of structural diversity among biologically relevant fluorophores[59–62]. The inherent brightness and tunable emission of CPPs makes them excellent potential scaffolds for new biological probes. Additionally, the common absorption shared by all CPPs has been predicted to enable multiplexed imaging[63], whereby multiple CPP fluorophores could, in principle, be excited simultaneously by a single laser to closely study complex biological phenomena. Inspired by this, we reported the synthesis of a bis(sulfonate) [8]CPP analogue[19] **3** (FIG. 2e), which, unlike its parent [8]CPP, is soluble in aqueous media and exhibits cellular uptake. The photophysical properties of **3** in both Me_2SO and phosphate-buffered saline (PBS) were found to be almost identical to those of [8]CPP (FIG. 2f,g). Compared with commercially available fluorescein[64], **3** exhibits moderately lower brightness, albeit with a substantially larger effective Stokes shift (41 nm for fluorescein versus 180 nm for **3**). Additionally, the emission intensity from **3** is unaffected by pH over a wide range (pH 3–11), whereas that from fluorescein drops off dramatically when the probe exists in acidic solution.

Nanohoop **3**, and most likely a range of nanohoop derivatives, are biologically compatible. Indeed, treating live HeLa cells with up to 25 μM of **3** revealed the latter not to be cytotoxic according to the WST-8 formazan reduction and Cell Counting Kit-8 (CCK-8) cell assay[64]. To test the utility of **3** as a biological probe, HeLa cells were incubated with **3** and the nuclear stain NucRed 647 for 1 h. After washing the cells, they exhibited clear permeation, with moderate colocalization in the cytosol and lower colocalization in the mitochondria and endoplasmic reticulum, but no colocalization with the nuclear dye[65]. Building on this, an azide-functionalized [8]CPP was synthesized and 'clicked' to an alkyne-functionalized folic acid group, which is effective in targeting cancer cells[66,67]. This folic-acid-functionalized [8]CPP is taken up in HeLa cells, suggesting that azide-functionalized nanohoops could provide a versatile scaffold for targeted cell imaging. The ultimate realization of such work would be the incorporation of azide groups into CPPs of various sizes, where one could 'click' distinct targeting groups to each one. This could potentially allow for simultaneous imaging of various targeted cellular structures by multiplexed imaging.

CPPs as solid-state emitters. Organic, small-molecule fluorophores are of great interest as solid-state emitters due to their synthetic tunability, solution processability and potential to be implemented into flexible devices[68–70]. However, the luminescence of many organic fluorophores is severely quenched on aggregation in the solid state[69]. By contrast, the bright emission of CPPs in solution is retained in the solid state[20,21,26] and, as discussed above, enables highly tunable emission. Additionally, the central pores of CPPs — not a feature found in traditional fluorophore scaffolds — offer a handle by which to tune emission[20]. A prime example of the exploitation of these properties in a functional capacity is [10]CPP·$2I_2$ (REF.[20]), an I_2 inclusion complex that is responsive to electrical stimuli[71–74] (FIG. 3a). Simply evaporating solvent from a solution of [10]CPP and I_2 affords crystalline [10]CPP·$2I_2$, which assumes a herringbone-like packing arrangement of [10]CPP molecules, each of which hosts two I_2 molecules. Application of a 500-mV stimulus to solid [10]CPP·$2I_2$ resulted not only in decreased electrical resistivity but also a broadened white-light emission profile that contrasts the green–blue emission prior to the stimulus (FIG. 3b). The underlying mechanisms of these phenomena are not yet understood but are most likely the result of structural changes in I_2 guest molecules — an effect that has been reported in numerous studies[75–77]. In support of this, the formation of anionic iodide chains within the nanohoop pores after the stimulus was identified using Raman spectroscopy and X-ray absorption near-edge spectroscopy (XANES). Raman spectra feature a stretching mode for I_2 (FIG. 3c) that is shifted from 207 cm^{-1} to 205 cm^{-1} upon stimulation, and the new bands at 112 cm^{-1} and 165 cm^{-1} have been ascribed to polyiodide chains[78]. Likewise, XANES data for [10]CPP·$2I_2$ (FIG. 3d) suggest that the antibonding orbitals in I_2 become populated after electrical stimulation, as evidenced by a decrease in intensity of a peak at 5,187 eV (representing the transition from the 2*s* to 5*p* antibonding orbital of I) and the emergence of a peak at 5,194 eV that has been previously observed for polyiodide chains[79]. Regardless of the mechanism behind the aforementioned emission broadening, achieving white-light emission is typically difficult[80,81], and doing so with a single-component system is relatively rare[80,81]. Perhaps more important than the results themselves, however, is the proof of concept that the uptake of guest molecules into a nanohoop can dramatically affect the system's photophysics. As we describe below, it turns out to be relatively common to observe fluorescence quenching in CPPs upon guest uptake[8,82]. This study shows that CPPs can be incorporated into complex host–guest systems with photophysical properties that can be tuned in a reversible, non-covalent manner by the stimulus-induced response of a guest.

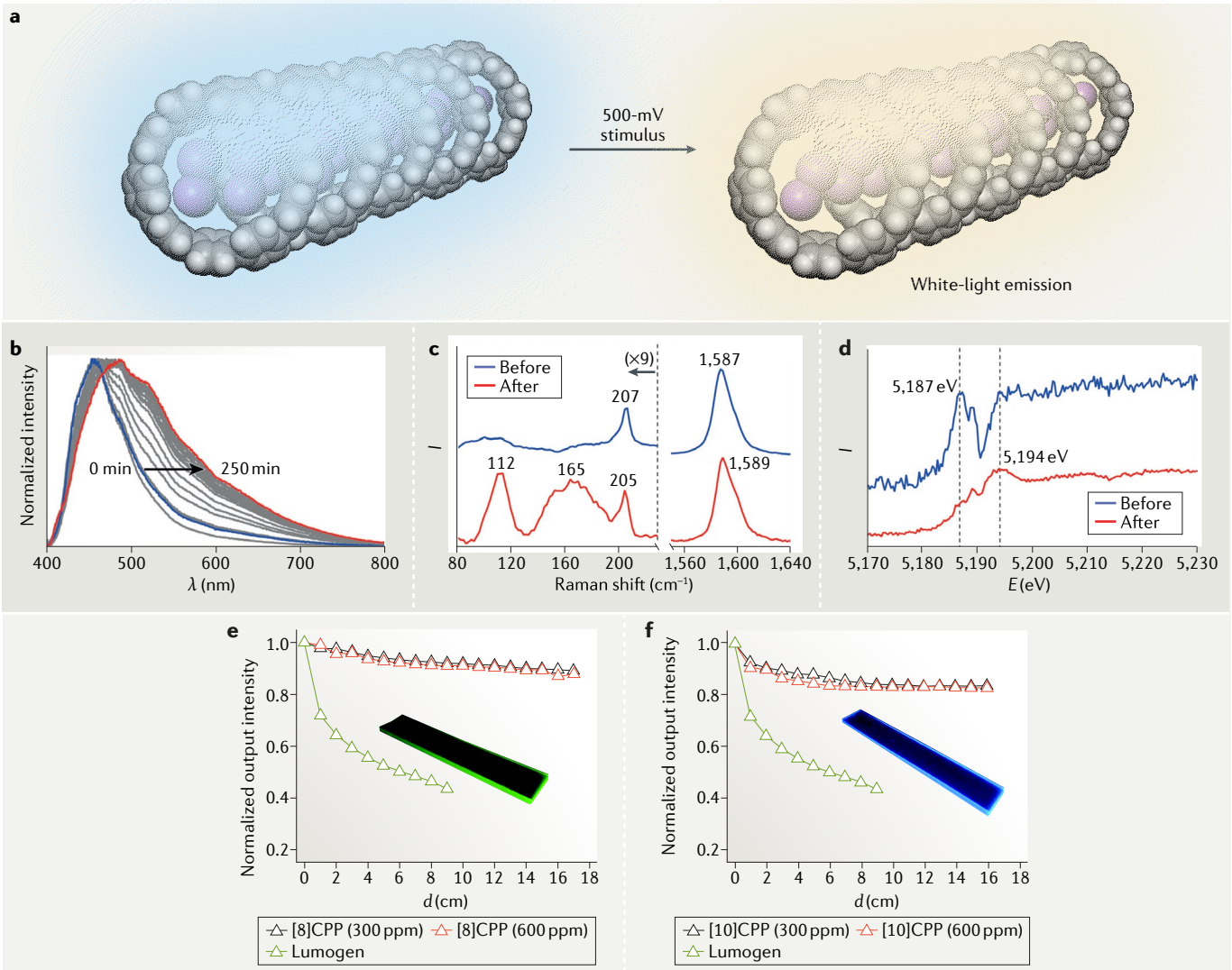

Fig. 3 | **Electrical and optical stimulation of cycloparaphenylenes. a** | Electrical stimulation of [10]CPP·2I_2 affords polyiodide chains and a change from blue to white emission. **b** | Emission broadening of [10]CPP·2I_2 as the electrical stimulus is maintained over 250 min. **c** | Raman spectra of [10]CPP·2I_2 before (blue) and after (red) the stimulus. **d** | X-ray absorption near-edge spectroscopy data of [10]CPP·2I_2 before (blue) and after (red) stimulus. **e** | Emission from luminescent solar concentrators containing [8]CPP at two concentrations, as well as the standard dye Lumogen, as a function of optical distance *d*. **f** | The same experiment as in part **e** carried out using [10]CPP. Parts **b**–**d** adapted with permission from REF.[20], Wiley-VCH. Parts **e** and **f** adapted with permission from REF.[21], Royal Society of Chemistry (https://doi.org/10.1039/C8CC09859J).

A more recent report describes the incorporation of CPPs into luminescent solar concentrator (LSC) devices[21], which are of interest due to their ability to efficiently convert optical power to electrical power[83–87]. CPPs are considered attractive for this purpose due to their large effective Stokes shifts (193 nm for [8]CPP and 128 nm for [10]CPP), which render photon reabsorption highly unlikely and, thus, improve LSC device efficiencies. Photoluminescence (PL) spectra were acquired for rectangular poly(methyl methacrylate) (PMMA) slabs doped with either [8]CPP or [10]CPP, revealing unique behaviour of the nanohoop fluorophores within this device geometry. The CPPs did indeed behave as effective LSC fluorophores, with solid-state emission very obviously concentrating at the edges of the PMMA slabs upon UV irradiation (365 nm) (FIG. 3e,f and insets). Additionally, photon reabsorption was found to be very minor (~10% loss) over a wide range of optical distances (0–18 cm, the length between the point of UV laser excitation and the point of emission detection) for both [8]CPP (FIG. 3e) and [10]CPP (FIG. 3f). In terms of efficiency, the nanohoop-based LSCs far outperform devices constructed using Lumogen R305 (REF.[88]) (FIG. 3e,f), a commercial perylene diimide marketed for the purposes of concentrating emitted light in devices such as LSCs. Along with the promising LSC performance, this study revealed important fundamental details regarding the solid-state emission of CPPs. The first and arguably most important detail is that nanohoop photophysics remain almost completely unchanged when the molecules are incorporated into a solid-state matrix such as PMMA, such that future CPP-based optical devices can

be predictably designed. Additionally, embedding CPPs within a solid slab of PMMA was found to moderately increase PL decay time, implying that immobilizing CPPs in solid media could provide a viable means to improve the efficiency of their solid-state PL devices.

CPPs in electronic applications

Recent studies indicated that fully conjugated, macrocyclic systems can outperform their linear analogues as active components in organic electronics[89]. This phenomenon is largely attributed to the radial geometries exhibited by certain conjugated macrocycles, which, like the 3D shape of fullerenes, allows for more intermolecular contacts than a comparable linear system[89]. Thus, the radially oriented π-systems of CPPs are expected to make them potentially attractive scaffolds for small-molecule-based electronics. Additionally, as discussed above, nanohoops offer an inherently tunable electronic scaffold in that their HOMO–LUMO gaps decrease with decreasing n[2–7] (FIG. 1a). Furthermore, numerous reports have established that the frontier molecular orbital energies of CPPs can be further tuned by functionalization reactions, such as the protonation or alkylation of pyridine-containing nanohoops, which afford charged donor–acceptor systems[90–92]. Although incorporating either one or two pyridine moieties into the [8]CPP backbone has little impact on frontier molecular orbital levels, methylating these systems to afford the analogous monocationic or dicationic *N*-methylpyridinium species results in a striking decrease in HOMO–LUMO gaps[92] (FIG. 4a). Approaches such as fluorination[17] and the inclusion of a 11,11,12,12-tetracyano-9,10-anthraquinodimethane (TCAQ) moiety into the nanohoop backbone[93] have also proven successful for tuning the electronic structures of CPP. In this way, CPPs are fascinating frameworks with predictably tunable frontier molecular orbitals, a highly sought after property in the field of organic electronics.

Although experiments interrogating the electronic capabilities of CPPs have been limited, interest in nanohoop-based electronics has been heightened by a number of theoretical reports probing their potential utility[94–97]. For example, the charge mobilities μ of crystalline CPP assemblies can be estimated[98] (FIG. 4b) using kinetic Monte Carlo simulations on solid-state assemblies of [5–12]CPP (extracted from their respective crystal structures)[8,39,42,99–103]. While the smaller nanohoops (n = 5–9) are predicted to exhibit low-to-moderate mobilities, [10–12]CPPs exhibit mobilities >1 and, thus, could offer formidable performance in organic semiconductors (FIG. 4b). Additionally, the theoretical charge-transport properties of both [5]CPP and [10]CPP can be compared with those of C_{60} (REF.[104]) in an effort to gauge where the bulk electronic properties of CPPs lie with respect to other curved, carbon-rich systems (FIG. 4c). The curved π–π contacts in all three systems are comparable, suggesting that they might have similar charge-transport capabilities. The calculations indicate that energetic disorder σ and reorganization energy λ dominate the mobilities. For [5]CPP, both energetic disorder (σ = 66 meV) and reorganization energy (λ = 261 meV) were predicted to be substantially higher than those of C_{60} (σ = 4 meV, λ = 135 meV), providing theoretical grounds for the two-orders-of-magnitude difference in mobility between [5]CPP ($\mu = 0.05\ cm^2\ V^{-1}\ s^{-1}$) and C_{60} ($\mu = 3.1\ cm^2\ V^{-1}\ s^{-1}$). Although the calculated reorganization energy of [10]CPP (λ = 98 meV) is markedly lower than that of C_{60}, its higher energetic disorder (σ = 42 meV) allows us to rationalize its moderately low charge mobility ($\mu = 0.83\ cm^2\ V^{-1}\ s^{-1}$). While experimental verification is still necessary, these results serve as excellent theoretical groundwork from which CPP-based electronic systems can be designed.

Numerous reports describe the redox properties of CPPs, which appear to be good electron acceptors. We have reported the isolation of $[8]CPP^{4-}$ (REF.[105]), $[6]CPP^{-}$ and $[6]CPP^{2-}$ (REF.[106]) as salts of ether-ligated Na^+ or K^+. These reduced nanohoop structures exhibit enhanced quinoidal character, which is evidenced by a shortening of the C–C bonds between phenylene moieties, and, in the case of $[8]CPP^{4-}$, considerable structural perturbations, resulting in an oval-like geometry. It should also be noted that both the trianions and the tetraanions of [6]CPP were detected using UV–visible spectroscopy but have, so far, eluded isolation[106]. CPPs can also be readily oxidized[107–111], with the monocations and dications of [n]CPP (n = 5, 6, 8, 10, 12) all being accessible by oxidizing the neutral species with $[NO]SbF_6$ or SbF_5 (REF.[110]). A wealth of fundamental information regarding these oxidized states has been reported, including the full charge delocalization in both $[n]CPP^{\bullet+}$ and $[n]CPP^{2+}$ species, and even the emergence of biradical character in $[10]CPP^{2+}$ and $[12]CPP^{2+}$ (REF.[110]). The weak, near-infrared emission from $[6–9]CPP^{2+}$ implies a drastic alteration in electronic structure upon oxidation[111], which has been attributed to in-plane aromaticity relevant to the oxidized CPP structures[109,111]. The strategy of altering CPP properties by reduction or oxidation is no doubt a fascinating prospect worthy of lengthier discussion, but the studies described above are also vital in furthering our understanding of nanohoops in the context of organic electronics. The ability of CPPs to readily accept or donate electrons bodes well for their use as potential bulk charge-transport materials. Additionally, the fundamental characterization of oxidized and reduced CPP structures that has been carried out thus far provides us with an approximate picture of how CPPs will behave on the molecular level when incorporated into electronics, allowing for better practical design of future CPP-based devices.

Despite numerous computational studies on the electronic applications of CPPs, only one experimental report describing properties of a CPP-based device exists. This is possibly a result of both the general difficulty in preparing these materials and the, until recently, relatively small number of researchers working in this area. A 2017 report described a streamlined synthesis of [10]CPP that enables access to a variety of tetraalkoxy[10]CPP derivatives[10]. Although the addition of alkoxy substituents to the [10]CPP backbone perturbed photophysics/electronics only to a small extent, the new [10]CPP derivatives exhibit substantially improved solubility in $CHCl_3$, making them amenable to solution-processing techniques[112], such as spin casting, for the preparation

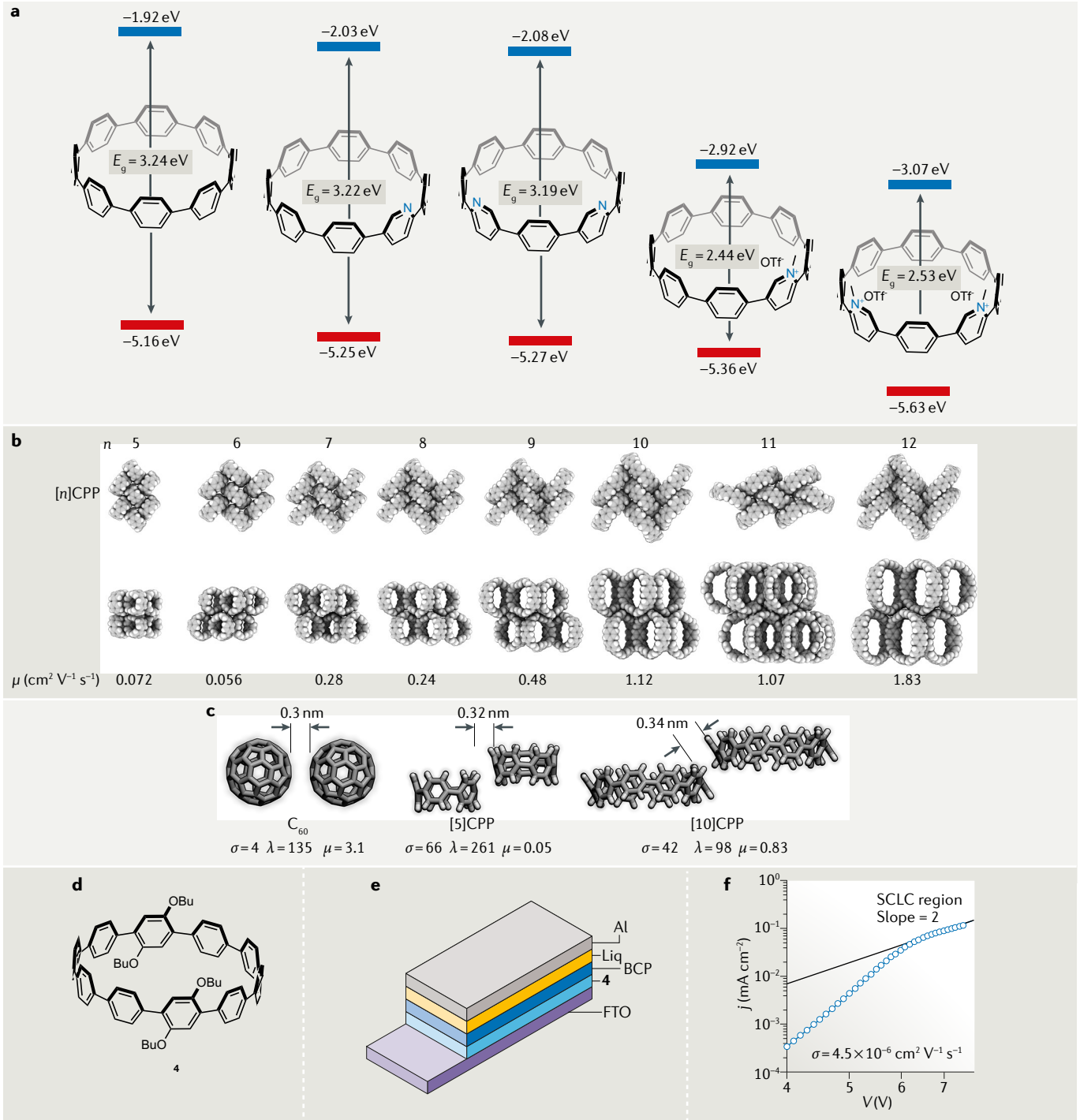

Fig. 4 | **Electronic properties of cycloparaphenylenes. a** | Highest occupied molecular orbital (HOMO) and lowest unoccupied molecular orbital (LUMO) energies and energy gaps $E_g = E_{HOMO} - E_{LUMO}$ for cycloparaphenylenes (from left to right) [8]CPP, aza[8]CPP, 1,15-diaza[8]CPP, *N*-methylaza[8]CPP triflate and *N*,*N*-dimethyl-1,15-diaza[8]CPP ditriflate. **b** | X-ray crystal structures of and calculated charge mobilities in [*n*]CPP (*n* = 5–12). **c** | Structures of dimers of C_{60}, [5]CPP and [10]CPP, along with intermolecular distances, calculated energetic disorders σ, reorganization energies λ and mobilities μ. **d** | Chemical structure of tetrabutoxy-functionalized [10]CPP **4**. **e** | The generic device architecture used for space-charge-limited current (SCLC) measurements. **f** | Acquiring SCLC data for devices constructed using **4** enables one to calculate the mobility. Part **f** adapted with permission from REF.[10], American Chemical Society.

of thin films. Of the [10]CPP derivatives synthesized, only tetrabutoxy[10]CPP (**4**, FIG. 4d) could be implemented into a vertical device architecture (FIG. 4e) that can allow for the space-charge-limited current (SCLC) to be measured[113]. Analysis of the current–voltage behaviour of the device revealed an electron mobility of 4.5×10^{-6} cm^2 V^{-1} s^{-1} (FIG. 4f), which, while a relatively low value, provides a baseline for future

studies of CPP electronics. The HOMO and LUMO energy levels of [10]CPP and **4** are comparable, so the massive, six-orders-of-magnitude discrepancy between the observed mobility for **4** and the theoretical mobility for the parent compound [10]CPP is instead rationalized in terms of differences in bulk morphology between the two systems. The theoretical study relied on the experimental X-ray crystal structure of [10]CPP and **4** presumably assumes a less-ordered solid-state structure on account of the conformationally flexible butoxy groups[114] (further characterization of these thin films would be required to confirm this). Single-crystal device measurements[115] on the [*n*]CPP (*n* = 5–12) series would, therefore, be intriguing, because such measurements could be directly compared with established theoretical work to produce a more complete picture of the fundamental bulk electronic properties of CPPs.

Fullerene@CPP systems. Fullerenes are ubiquitous in organic electronics because their anomalously low LUMO energies mean that their anions are relatively stable. This useful *n*-type behaviour is complemented by their ability to be readily incorporated into device architectures[116,117]. However, tuning fullerene properties by functionalization is a non-trivial task. As a result, supramolecular approaches to altering fullerene behaviour are attractive methods to prepare novel, fullerene-based systems[118]. A particularly notable example of this is the linear encapsulation of C_{60} by CNTs to give 'CNT peapods' (REFS[119,120]), in which there is enhanced electronic communication between the fullerene guest molecules[121]. Similarly, the linear encapsulation of C_{60} within $ExBox_2^{4+}$ (an extended-bipyridinium-containing cyclophane) affords $C_{60}\subset ExBox_2^{4+}$, which has the desirable electrical conductivity of C_{60} without the air sensitivity and moisture sensitivity of bulk C_{60} anions[122]. The CNT-like inner pores of CPPs offer a unique, electron-rich environment capable of encapsulating fullerenes[8,82], making CPPs an ideal platform to tune fullerene behaviour. The first evidence of a fullerene@CPP system came in 2011 with the report of a C_{60}@[10]CPP complex[82], which is stable on account of the remarkably high binding constant ($2.79\times10^6\ M^{-1}$). Shortly after this, we reported the first crystal structure of C_{60}@[10]CPP, which reflects the beautiful π–π complementarity of the two components[8]. The formation of C_{60}@[10]CPP is accompanied by a dramatic quenching of [10]CPP emission, suggesting photophysical and electronic consequences of binding. In 2013, C_{70} was shown to be captured by both [10]CPP and [11]CPP, expanding the scope of fullerene@CPP host–guest chemistry[123]. Following this, inspired by the unique electronic and magnetic properties of metallofullerenes[124–127], came syntheses of ($La@C_{82}$)@[11]CPP[128] and ($Li^+@C_{60}$)@[10]CPP[129], respectively. Interestingly, both systems exhibit varying degrees of charge-transfer behaviour, a property not observed for the analogous all-hydrocarbon fullerene@CPP complexes. Although outside of the scope of this Review, we note that fullerenes exhibit unique frictionless rotation within nanohoop pores[130–132], and these nanoscale 'bearings' might, one day, be used as components of nanoscale machinery.

The propensity of fullerenes to accept electrons has made them popular for implementation into small-molecule charge-transfer systems. Among the most studied of these are fullerene–porphyrin dyads, in which an excited porphyrin moiety can transfer an electron to an appended fullerene[133–135]. The syntheses of these systems are typically non-trivial, as they require a covalent linkage between the porphyrin and fullerene components. Instead, a clever use of fullerene@CPP host–guest chemistry has afforded porphyrin-functionalized [10]CPP (**5**, FIG. 5a), which, upon binding of C_{60} within the appended [10]CPP, allowed for through-space charge transfer between the porphyrin and fullerene without the need for fullerene functionalization[22]. Transient absorption spectra of C_{60}@**5** have features at ~670 nm and 1,090 nm (FIG. 5b,c) assigned to the singly oxidized porphyrin[136] and singly reduced C_{60} (REF.[137]), respectively, that are part of a metastable, charge-separated state $C_{60}^{\bullet-}$@$\mathbf{5}^{\bullet+}$ that has a lifetime of 4.3 ns. This contrasts the behaviour of uncomplexed **5**, in which the porphyrin excited state eventually undergoes intersystem crossing to afford an excited triplet state. Charge separation has also been observed for several other fullerene derivatives, which exhibit comparable lifetimes when irradiated. The study also explored the use of a fullerene dimer $(C_{60})_2$ in this system. It was found that, by varying stoichiometry and concentration, either a 1:1 complex $(C_{60})_2$@**5** or a 2:1 complex **5**@$(C_{60})_2$@**5** could be formed (FIG. 5d). For the 1:1 complex, the formation of two distinct fullerene monoanions was observed, one with a lifetime of ~2.5 ns and another with a greatly extended lifetime of ~13.4 ns (FIG. 5d). The longer-lived anion is thought to have the negative charge on the non-complexed fullerene, which is situated farther away from the porphyrin moiety of **5**. Particularly surprising was the discovery of a ~541-ns lifetime for the charge-separated state of the 2:1 complex **5**@$(C_{60})_2$@**5**, which was attributed to charge delocalization in the system (FIG. 5d). Overall, this study suggests that altering the relative spatial arrangement of donor and acceptor in this [10]CPP-based supramolecular system, perhaps by lengthening of the phenylene linker of **6**, might allow for unprecedented control over charge-separated state lifetimes in fullerene–porphyrin charge-transfer systems.

One of the more popular uses of fullerenes is as the *n*-type component (electron acceptor) in photovoltaic systems[116]. Thus, a CPP derivative with appropriately tuned frontier molecular orbital levels could be used as an electron-donor component in conjunction with a fullerene to afford a unique, supramolecular photovoltaic system. Despite this prospect, electronic applications of fullerene@CPP systems have been relatively unexplored from a practical viewpoint. An exception to this is a very recent report describing the first implementation of fullerene@CPP complexes into functional device architectures[23]. Two new [10]CPP derivatives were prepared: one containing a tribenzo[*fj*,*ij*,*rst*]pentaphene (TBP) group (**6**, FIG. 5e) and another with a hexa-*peri*-hexabenzocoronene (HBC) moiety embedded in the nanohoop backbone (**7**, FIG. 5e). The LUMO energies of both **6** and **7** are lower than that of the parent [10]CPP, suggesting that C_{60} may engage in faster

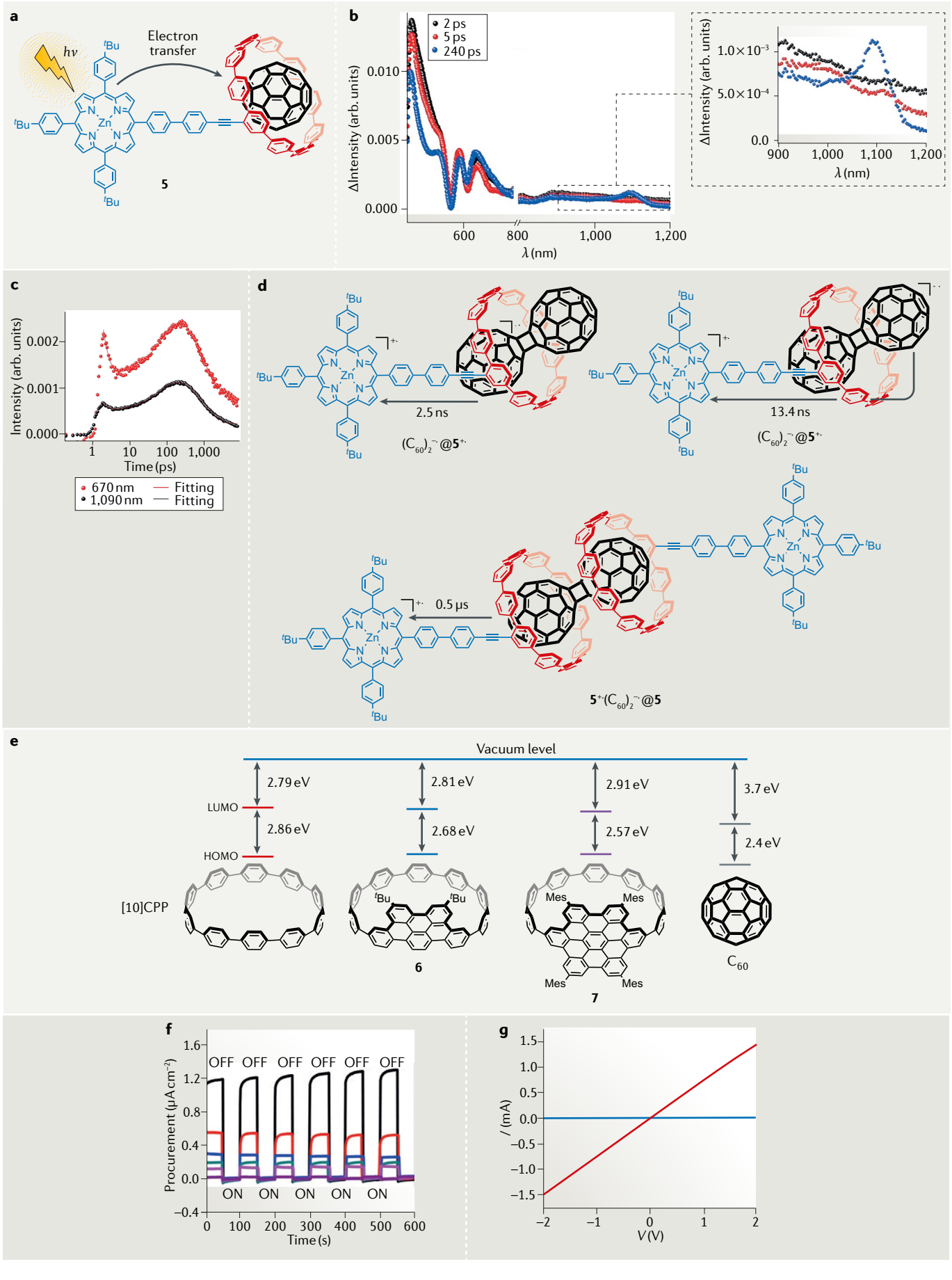
a
Electron transfer
hν
tBu
Zn
5
b
2 ps
5 ps
240 ps
ΔIntensity (arb. units)
0.010
0.005
0.000
600
800
1,000
1,200
λ (nm)
1.0×10−3
5.0×10−4
0.0
900
1,000
1,100
1,200
c
Intensity (arb. units)
0.002
0.001
0.000
1
10
100
1,000
Time (ps)
670 nm
1,090 nm
Fitting
Fitting
d
2.5 ns
(C60)2•−@5•+
13.4 ns
(C60)2•−@5•+
0.5 μs
5•+(C60)2•−@5
e
Vacuum level
2.79 eV
LUMO
2.86 eV
HOMO
[10]CPP
2.81 eV
2.68 eV
6
2.91 eV
2.57 eV
Mes
7
3.7 eV
2.4 eV
C60
f
Procurement (μA cm−2)
1.6
1.2
0.8
0.4
0.0
−0.4
OFF
ON
0
100
200
300
400
500
600
Time (s)
g
I (mA)
1.5
1.0
0.5
0.0
−0.5
−1.0
−1.5
−2
−1
0
1
2
V (V)

◀ Fig. 5 | **Electron transfer involving cycloparaphenylenes. a** | The porphyrin-appended [10]CPP host **5** can bind C_{60} to form a charge-transfer complex. **b** | Differential absorption spectra of C_{60}**@5** in PhCN acquired in pump–probe experiments (430 nm, 500 nJ). **c** | Time–absorption profiles and fits of the absorption fingerprints of the C_{60} radical anion at 1,090 nm (black) and the porphyrin radical cation at 670 nm (red). **d** | Lifetimes of charge-separated states of $(C_{60})_2$**@5** and **5**@$(C_{60})_2$**@5**. **e** | Highest occupied molecular orbital (HOMO) and lowest unoccupied molecular orbital (LUMO) energies (relative to vacuum) of [10]CPP, nanohoop **6**, nanohoop **7** and C_{60}. **f** | Photocurrent response of spin-coated films of C_{60}**@7** (black), **7** (red), C_{60}**@6** (dark blue), **6** (light blue), [10]CPP@C_{60} (pink) and [10]CPP (purple). **g** | *I*–*V* profiles of C_{60}**@7** before (blue) and during (red) photoirradiation. Parts **b** and **c** adapted with permission from REF.[22], Wiley-VCH. Parts **f** and **g** adapted with permission from REF.[23], Wiley-VCH.

electron transfer when complexed to **6** or **7** than if complexed to [10]CPP (FIG. 5e). The binding constants of C_{60} to nanohoops **6** and **7** ($K_a = 3.34 \times 10^6$ mol l^{-1} for **6** and $K_a = 2.33 \times 10^7$ mol l^{-1} for **7**) are higher than that of C_{60} to [10]CPP due to the smaller π-conjugated surface area of the latter (FIG. 5f). One can probe the electronic properties of these host–guest systems by spin-coating them as films onto fluorine-doped tin oxide (FTO) working electrodes. These electrodes can then be irradiated and it is possible to measure photocurrent that may arise from excited-state charge transfer from the nanohoop to the fullerene. Notably, photocurrent was observed for C_{60}**@6**, C60@**7** and C_{60}@[10]CPP, as well as the free nanohoops **6** and **7**, with no photocurrent observed for free [10]CPP (FIG. 5f). Of these systems, **7** was found to have the greatest photocurrent response, presumably due to the lower LUMO energy of **7** and, thus, greater ease with which it can transfer electrons to the LUMO of C_{60}. Further analysis of the current–voltage response of C_{60}**@7** revealed a 1,000-fold increase in current upon photoirradiation (FIG. 5g). Similar to fullerene**@5** systems[22], transient absorption spectroscopy revealed that both C_{60}**@6** and C_{60}**@7** form metastable, charge-separated states upon excitation and, thus, represent supramolecular donor–acceptor charge-transfer systems. Overall, the superior performance of the C_{60}**@7** complex in the generation of photocurrent implies that nanohoops can indeed be precisely tuned to afford ideal hosts for the construction of high-performance photovoltaics.

CPPs as building blocks for carbon nanomaterials

CPPs were originally envisioned as potential templates for the growth of homochiral CNTs, a prospect that has yet to be realized, despite promising preliminary results[138]. As an alternative to using CPPs as precursors to carbon nanomaterials, research is rapidly emerging regarding the use of bulk CPP systems as novel materials in their own right. One of the first such studies reported that [12]CPP behaves as a soft, porous, molecular solid[24]. The pores of bulk [12]CPP are inaccessible to N_2 and CO_2 gas at 77 K and 87 K, respectively, presumably due to the material's dense, herringbone-like packing[99] (FIG. 6a). Although no N_2 was adsorbed at 195 K, this higher temperature allowed for CO_2 uptake corresponding to a Brunauer–Emmett–Teller surface area of 503 m^2 g^{-1} — a relatively high value for bulk assemblies of intrinsically porous macrocycles[140,141]. The increased molecular motion at elevated temperatures increases the average pore size of bulk [12]CPP, which, apparently, is selective for CO_2 at this temperature[142]. The material also adsorbs MeOH, EtOH, cyclohexane and *n*-hexane vapour, although it does not take up H_2O because H_2O forms stable, hydrogen-bonded aggregates that were thought to be too large for the small [12]CPP pores. The bulk [12]CPP material was also found to be soft in the sense that its solid-state morphology could change to accommodate guests. For example, powder X-ray diffraction (XRD) measurements during MeOH uptake revealed clear changes in peak pattern and intensity upon increasing MeOH uptake (FIG. 6b,c). Importantly, this process was found to be reversible, with the [12]CPP diffraction pattern returning to its initial state upon desorption. These XRD data served as the basis for a stepwise mechanistic proposal, in which MeOH uptake involves multiple distinct structural deformations, ultimately resulting in the uptake of ~9 molecules per nanohoop. The ability of bulk CPP samples to adsorb various analytes opens the door to myriad potential studies. For example, because guests can alter the emissive properties of CPPs, bulk CPP samples could be used as dynamic sensors that exhibit altered fluorescence upon analyte uptake.

Self-assembled carbon nanomaterials have begun to see use as novel materials to target specific cellular sites[143–145]. However, the design of these materials is difficult because most biomaterials enter cells by endocytosis and localize in endosomes before undergoing degradation in lysosomes[146,147]. Therefore, it remains a challenge to find supramolecular synthons from which biomaterials can be self-assembled. Due to their low cytotoxicity[18] and bright emission, CPPs represent excellent candidates for the fabrication of new functional biomaterials. This is further supported by a recent observation, using cryo-transmission electron microscopy, of vesicle-like [10]CPP aggregates in THF or Me_2SO upon the addition of H_2O[25] (FIG. 6d,e). The size of these vesicles could be loosely controlled by varying the cosolvent:H_2O ratios at [10]CPP constant concentration. To explore the uptake of the [10]CPP vesicles in cells, vesicles of 78 nm in mean diameter were co-incubated with human alveolar basal epithelial cells (A549) and mouse colon cancer cells (CT26) in Me_2SO–PBS (1:99). [10]CPP vesicle uptake was observed in both cell lines, with bright-blue emission from [10]CPP appearing primarily in the cytoplasm, with none coming from the nucleus (FIG. 6f). Interestingly, vesicle uptake was observed at both 4 °C and 37 °C, implying that the uptake mechanism is independent of both energy and temperature. Likewise, cellular uptake of [10]CPP vesicles was found to be unaffected by a variety of endocytosis inhibitors, suggesting that cellular permeation by the vesicles does not occur through an endocytosis-dependent mechanism. Cell-viability experiments revealed IC_{50} values of 7.2 μg^{-1} and 4.9 μg ml^{-1} for the A549 and CT26 cell lines, respectively. These preliminary results, which implicate a non-endocytotic uptake mechanism, encourage the further exploration of nanohoops as building blocks for functional self-assembled biomaterials.

The above CPP vesicles represent a unique case of CPP self-assembly induced by an external stimulus (the presence of H_2O). We have taken a different approach and chosen to focus on the programmed self-assembly of functionalized nanohoops. Inspired by the idea of using

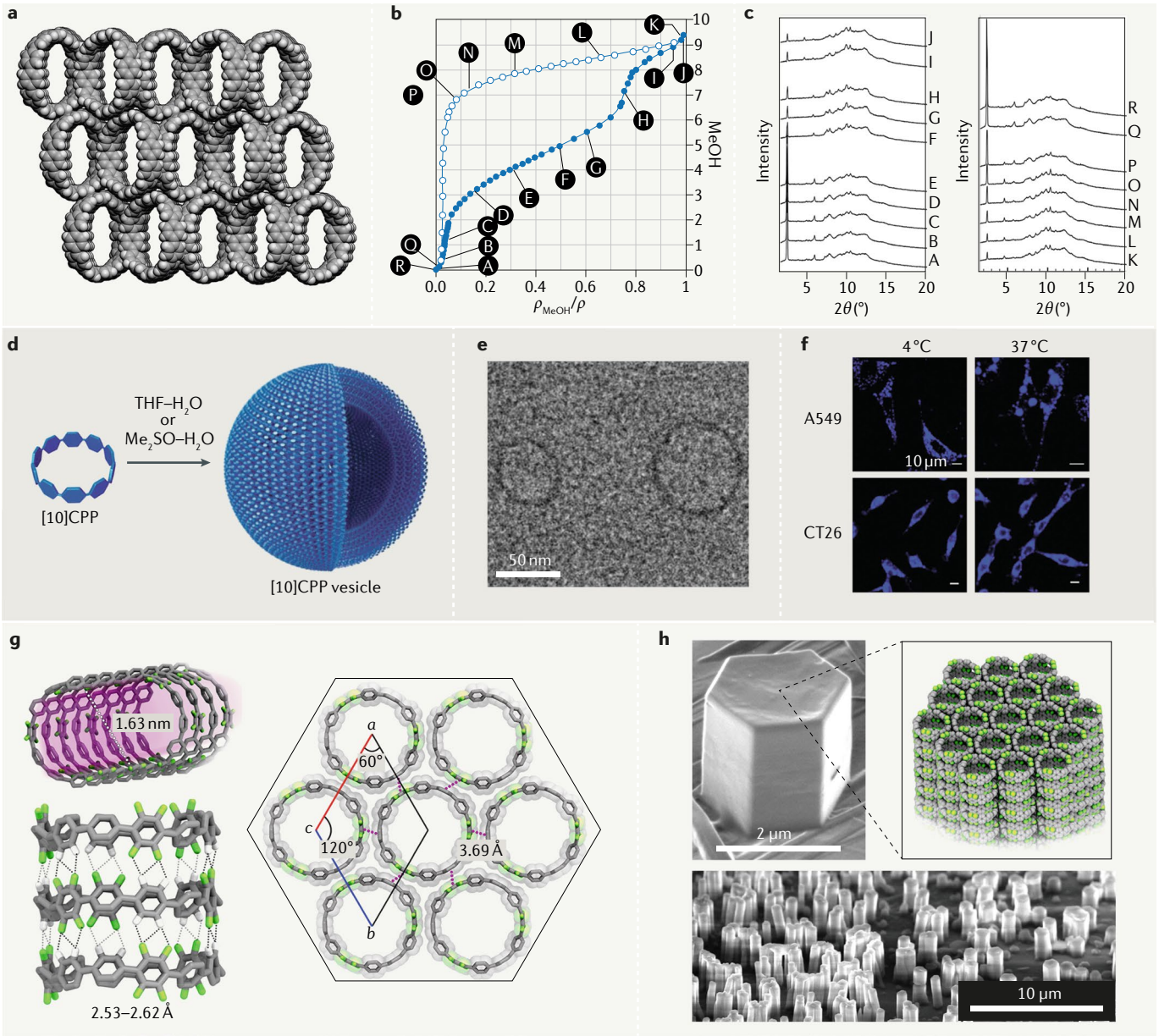

Fig. 6 | **Cycloparaphenylenes can serve as building blocks for nanomaterials. a** | Crystals of the cycloparaphenylene [12]CPP feature pores that are available to guest molecules. **b** | Adsorption (filled circles) and desorption (open circles) isotherms for MeOH and [12]CPP. **c** | In situ powder X-ray diffraction measurements of [12]CPP during MeOH uptake. The letters correspond to points in the isotherms in **b**. **d** | Schematic of the proposed structure of a vesicle formed by self-assembly of [10]CPP in THF–H_2O or Me_2SO–H_2O solvent mixtures. **e** | Cryo-transmission electron micrograph of [10]CPP vesicles. **f** | Fluorescence microscope images of [10]CPP vesicles within A549 and CT26 cells at 4 °C and 37 °C. **g** | X-ray crystal structure of 3F[12]CPP, highlighting the 1.63-nm channels (top left), C–H···F interactions (bottom left) and arene–perfluoroarene interactions (right). **h** | Scanning electron microscopy images of the hexagonal pillars formed by 3F[12]CPP drop-casted onto highly ordered pyrolytic graphite, with the inset showing the proposed vertically aligned arrangement of nanohoops. Parts **b** and **c** adapted with permission from REF.[24], Royal Society of Chemistry (https://doi.org/10.1039/C6SC00092D). Parts **d**–**f** adapted with permission from REF.[25], Royal Society of Chemistry (https://doi.org/10.1039/C9BM00347A). Parts **g** and **h** reproduced with permission from REF.[26], American Chemical Society.

CPPs in the size-selective construction of CNTs, we hypothesized that it would be possible to construct non-covalent CNT mimics from appropriately functionalized CPPs. Towards this, we presented the synthesis and characterization of the nanohoop 3F[12]CPP, which features three 2,3,5,6-tetrafluorophenylenes, each spaced by a regular triphenylene group[26] (FIG. 6g). The fluorinated nanohoops were designed to self-assemble into cylinders, driven by a combination of C–H···F hydrogen bonding[148] and arene–perfluoroarene interactions[149–152]. XRD analysis revealed that 3F[12]CPP packs into perfectly linear nanotube-like channels in the vertical direction and perfect hexagonal sheets in the lateral direction. Thirty-six C–H···F interactions (2.53–2.62 Å) per hoop

were found to guide vertical assembly, while six arene–perfluoroarene interactions (3.69 Å) per hoop appeared to dominate assembly horizontally. The resulting CNT-like channels are all 1.63 nm in diameter, underscoring the promise of the present approach to preparing functional CNT mimics with atomic-level control.

The hexagonal 3F[12]CPP nanowires can also be grown through mild solution casting onto highly ordered pyrolytic graphite (HOPG; FIG. 6h). In this way, one can construct hexagonal prismatic pillars, and scanning electron microscopy (SEM) indicates that these pillars span, on average, ~1–2 μm in height and width. The hexagonal pillars are presumed to comprise vertically aligned arrays of 3F[12]CPP, which are evident in the crystal packing in the X-ray structure (FIG. 6h). The alignment of these pillars on HOPG is tentatively attributed to lattice matching because the in-plane lattice constant of graphene is a factor of 8 less than that of 3F[12]CPP[153]. The hexagonal pillars are quite flexible, and many oscillate like cantilever beams during SEM imaging. Additionally, fluorescence microscopy revealed the pillars to be bright-blue emitters, establishing that the emissive properties of 3F[12]CPP are retained in the solid state. We intend to further study the utility of these CNT mimics, particularly in view of exploiting the functionality of their inner channels. The hydrophobic, electron-rich channels of CNTs exhibit fast mass and H^+ transport[154,155], albeit with strong dependence on the channel diameter. Applications of such transport have been hampered by the lack of methodologies for synthesizing CNTs size selectively[156,157], but the recent size-selective syntheses described above will undoubtedly afford CNT mimics with the desired transport properties. Overall, the fluorination-based approach is applicable to CPPs of other sizes[17], and particularly appealing would be the synthesis of a fluorinated [10]CPP analogue, which could, in principle, be employed to construct non-covalent CNT peapod mimics through linear C_{60} alignment.

Conclusions and outlook

In just a decade, CPPs have gone from being synthetic curiosities to readily accessible materials with highly tunable properties. The syntheses of CPPs are motivated by a broad scope of exciting applications, ranging from solid-state nanomaterials to biological imaging. The bright, tunable emission from CPPs in solution and in the solid state is expected to be useful in next-generation display technologies and new, biologically relevant fluorophores and sensors, among other applications. Likewise, the ability to tune the electronic structure of CPPs by covalent functionalization or complexation with guest molecules such as fullerenes is predicted to be advantageous in areas such as organic photovoltaics. Finally, the self-assembly of CPPs, which has attracted little attention until recently, has already proved to be useful to form microporous materials, biologically relevant nanomaterials and atomically precise CNT mimics. With such a wide breadth of potential uses already beginning to emerge, we foresee carbon nanohoops and their derivatives evolving into ubiquitous, atom-precise scaffolds in carbon-based nanomaterials.

Published online: 29 October 2019

1. Jasti, R., Bhattacharjee, J., Neaton, J. B. & Bertozzi, C. R. Synthesis, characterization, and theory of [9]-, [12]-, and [18]cycloparaphenylene: carbon nanohoop structures. *J. Am. Chem. Soc.* **130**, 17646–17647 (2008).
2. Darzi, E. R., Sisto, T. J. & Jasti, R. Selective syntheses of [7]–[12]cycloparaphenylenes using orthogonal Suzuki–Miyaura cross-coupling reactions. *J. Org. Chem.* **77**, 6624–6628 (2012).
3. Iwamoto, T., Watanabe, Y., Sakamoto, Y., Suzuki, T. & Yamago, S. Selective and random syntheses of [*n*]cycloparaphenylenes (*n* = 8–13) and size dependence of their electronic properties. *J. Am. Chem. Soc.* **133**, 8354–8361 (2011).
4. Segawa, Y. et al. Combined experimental and theoretical studies on the photophysical properties of cycloparaphenylenes. *Org. Biomol. Chem.* **10**, 5979–5984 (2012).
5. Li, P., Sisto, T. J., Darzi, E. R. & Jasti, R. The effects of cyclic conjugation and bending on the optoelectronic properties of paraphenylenes. *Org. Lett.* **16**, 182–185 (2014).
6. Fujitsuka, M., Iwamoto, T., Kayahara, E., Yamago, S. & Majima, T. Enhancement of the quinoidal character for smaller [*n*]cycloparaphenylenes probed by Raman spectroscopy. *ChemPhysChem* **14**, 1570–1572 (2013).
7. Hines, D. A., Darzi, E. R., Jasti, R. & Kamat, P. V. Carbon nanohoops: excited singlet and triplet behavior of [9]- and [12]-cycloparaphenylene. *J. Phys. Chem. A* **118**, 1595–1600 (2014).
8. Xia, J., Bacon, J. W. & Jasti, R. Gram-scale synthesis and crystal structures of [8]- and [10]CPP, and the solid-state structure of C_{60}@[10]CPP. *Chem. Sci.* **3**, 3018–3021 (2012).
9. Kayahara, E., Patel, V. K., Xia, J., Jasti, R. & Yamago, S. Selective and gram-scale synthesis of [6]cycloparaphenylene. *Synlett* **26**, 1615–1619 (2015).
10. Kayahara, E. et al. Gram-scale syntheses and conductivities of [10]cycloparaphenylene and its tetraalkoxy derivatives. *J. Am. Chem. Soc.* **139**, 18480–18483 (2017).
11. Li, P., Wong, B. M., Zakharov, L. N. & Jasti, R. Investigating the reactivity of 1,4-anthracene-incorporated cycloparaphenylene. *Org. Lett.* **18**, 1574–1577 (2016).
12. Van Raden, J. M., Louie, S., Zakharov, L. N. & Jasti, R. 2,2′-Bipyridyl-embedded cycloparaphenylenes as a general strategy to investigate nanohoop-based coordination complexes. *J. Am. Chem. Soc.* **139**, 2936–2939 (2017).
13. Evans, P. J., Zakharov, L. N. & Jasti, R. Synthesis of carbon nanohoops containing thermally stable cis azobenzene. *J. Photochem. Photobiol. A Chem.* **382**, 111878 (2019).
14. Matsui, K., Segawa, Y. & Itami, K. Synthesis and properties of cycloparaphenylene-2,5-pyridylidene: a nitrogen-containing carbon nanoring. *Org. Lett.* **14**, 1888–1891 (2012).
15. Tran-Van, A.-F. et al. Synthesis of substituted [8]cycloparaphenylenes by [2 + 2 + 2] cycloaddition. *Org. Lett.* **16**, 1594–1597 (2014).
16. Kubota, N., Segawa, Y. & Itami, K. η^6-Cycloparaphenylene transition metal complexes: synthesis, structure, photophysical properties, and application to the selective monofunctionalization of cycloparaphenylenes. *J. Am. Chem. Soc.* **137**, 1356–1361 (2015).
17. Hashimoto, S. et al. Synthesis and physical properties of polyfluorinated cycloparaphenylenes. *Org. Lett.* **20**, 5973–5976 (2018).
18. Van Raden, J. M., White, B. M., Zakharov, L. N. & Jasti, R. Nanohoop rotaxanes via active metal template syntheses and their potential in sensing applications. *Angew. Chem. Int. Ed.* **58**, 7341–7345 (2019).
19. White, B. M. et al. Expanding the chemical space of biocompatible fluorophores: nanohoops in cells. *ACS Cent. Sci.* **4**, 1173–1178 (2018).
20. Ozaki, N. et al. Electrically activated conductivity and white light emission of a hydrocarbon nanoring–iodine assembly. *Angew. Chem. Int. Ed.* **56**, 11196–11202 (2017).
21. Della Sala, P. et al. First demonstration of the use of very large Stokes shift cycloparaphenylenes as promising organic luminophores for transparent luminescent solar concentrators. *Chem. Commun.* **55**, 3160–3163 (2019).
22. Xu, Y. et al. A supramolecular [10]CPP junction enables efficient electron transfer in modular porphyrin–[10]CPP⊃fullerene complexes. *Angew. Chem. Int. Ed.* **57**, 11549–11553 (2018).
23. Huang, Q. et al. Photoconductive curved-nanographene/fullerene supramolecular heterojunctions. *Angew. Chem. Int. Ed.* **58**, 6244–6249 (2019).
24. Sakamoto, H. et al. Cycloparaphenylene as a molecular porous carbon solid with uniform pores exhibiting adsorption-induced softness. *Chem. Sci.* **7**, 4204–4210 (2016).
25. Tang, H. et al. Nanoscale vesicles assembled from non-planar cyclic molecules for efficient cell penetration. *Biomater. Sci.* **7**, 2552–2558 (2019).
26. Leonhardt, E. J. et al. A bottom-up approach to solution-processed, atomically precise graphitic cylinders on graphite. *Nano Lett.* **18**, 7991–7997 (2018).
27. Darzi, E. R. & Jasti, R. The dynamic, size-dependent properties of [5]–[12]cycloparaphenylenes. *Chem. Soc. Rev.* **44**, 6401–6410 (2015).
28. Golder, M. R. & Jasti, R. Syntheses of the smallest carbon nanohoops and the emergence of unique physical phenomena. *Acc. Chem. Res.* **48**, 557–566 (2015).
29. Lewis, S. E. Cycloparaphenylenes and related nanohoops. *Chem. Soc. Rev.* **44**, 2221–2304 (2015).
30. Wu, D., Cheng, W., Ban, X. & Xia, J. Cycloparaphenylenes (CPPs): an overview of synthesis, properties, and potential applications. *Asian J. Org. Chem.* **7**, 2161–2181 (2018).
31. Majewski, M. A. & Ste˛pien´, M. Bowls, hoops, and saddles: synthetic approaches to curved aromatic molecules. *Angew. Chem. Int. Ed.* **58**, 86–116 (2019).
32. Povie, G., Segawa, Y., Nishihara, T., Miyauchi, Y. & Itami, K. Synthesis of a carbon nanobelt. *Science* **356**, 172–175 (2017).
33. Povie, G., Segawa, Y., Nishihara, T., Miyauchi, Y. & Itami, K. Synthesis and size-dependent properties of

[12], [16], and [24]carbon nanobelts. *J. Am. Chem. Soc.* **140**, 10054–10059 (2018).
34. Segawa, Y. et al. Topological molecular nanocarbons: all-benzene catenane and trefoil knot. *Science* **365**, 272–276 (2019).
35. Banerjee, M., Shukla, R. & Rathore, R. Synthesis, optical, and electronic properties of soluble poly-*p*-phenylene oligomers as models for molecular wires. *J. Am. Chem. Soc.* **131**, 1780–1786 (2009).
36. Segawa, Y., Omachi, H. & Itami, K. Theoretical studies on the structures and strain energies of cycloparaphenylenes. *Org. Lett.* **12**, 2262–2265 (2010).
37. Chen, H., Golder, M. R., Wang, F., Jasti, R. & Swan, A. K. Raman spectroscopy of carbon nanohoops. *Carbon* **67**, 203–213 (2014).
38. Adamska, L. et al. Self-trapping of excitons, violation of Condon approximation, and efficient fluorescence in conjugated cycloparaphenylenes. *Nano Lett.* **14**, 6539–6546 (2014).
39. Evans, P. J., Darzi, E. R. & Jasti, R. Efficient room-temperature synthesis of a highly strained carbon nanohoop fragment of buckminsterfullerene. *Nat. Chem.* **6**, 404–408 (2014).
40. Xia, J. & Jasti, R. Synthesis, characterization, and crystal structure of [6]cycloparaphenylene. *Angew. Chem. Int. Ed.* **51**, 2474–2476 (2012).
41. Lovell, T. C., Colwell, C. E., Zakharov, L. N. & Jasti, R. Symmetry breaking and the turn-on fluorescence of small, highly strained carbon nanohoops. *Chem. Sci.* **10**, 3786–3790 (2019).
42. Yamago, S., Watanabe, Y. & Iwamoto, T. Synthesis of [8]cycloparaphenylene from a square-shaped tetranuclear platinum complex. *Angew. Chem. Int. Ed.* **49**, 757–759 (2010).
43. Jasti, R. & Bertozzi, C. R. Progress and challenges for the bottom-up synthesis of carbon nanotubes with discrete chirality. *Chem. Phys. Lett.* **494**, 1–7 (2010).
44. Sisto, T. J., Golder, M. R., Hirst, E. S. & Jasti, R. Selective synthesis of strained [7]cycloparaphenylene: an orange-emitting fluorophore. *J. Am. Chem. Soc.* **133**, 15800–15802 (2011).
45. Kayahara, E., Patel, V. K. & Yamago, S. Synthesis and characterization of [5]cycloparaphenylene. *J. Am. Chem. Soc.* **136**, 2284–2287 (2014).
46. Balzani, V., Credi, A., Francisco, M. & Stoddart, J. F. Artificial molecular machines. *Angew. Chem. Int. Ed.* **39**, 3348–3391 (2000).
47. Bruns, C. J. & Stoddart, J. F. *The Nature of the Mechanical Bond: From Molecules to Machines* (Wiley-VCH, 2016).
48. Langton, M. J. & Beer, P. D. Rotaxane and catenane host structures for sensing charged guest species. *Acc. Chem. Res.* **47**, 1935–1949 (2014).
49. Denis, M., Qin, L., Turner, P., Jolliffe, K. A. & Goldup, S. M. A fluorescent ditopic rotaxane ion-pair host. *Angew. Chem. Int. Ed.* **57**, 5315–5319 (2018).
50. Denis, M., Pancholi, J., Jobe, K., Watkinson, M. & Goldup, S. M. Chelating rotaxane ligands as fluorescent sensors for metal ions. *Angew. Chem. Int. Ed.* **57**, 5310–5314 (2018).
51. Sagara, Y. et al. Rotaxanes as mechanochromic fluorescent force transducers in polymers. *J. Am. Chem. Soc.* **140**, 1584–1587 (2018).
52. Movsisyan, L. D. et al. Polyyne rotaxanes: stabilization by encapsulation. *J. Am. Chem. Soc.* **138**, 1366–1376 (2016).
53. Arunkumar, E., Forbes, C. C., Noll, B. C. & Smith, B. D. Squaraine-derived rotaxanes: sterically protected fluorescent near-IR dyes. *J. Am. Chem. Soc.* **127**, 3288–3289 (2005).
54. Aucagne, V., Hänni, K. D., Leigh, D. A., Lusby, P. J. & Walker, D. B. Catalytic "click" rotaxanes: a substoichiometric metal-template pathway to mechanically interlocked architectures. *J. Am. Chem. Soc.* **128**, 2186–2187 (2006).
55. Denis, M. & Goldup, S. M. The active template approach to interlocked molecules. *Nat. Rev. Chem.* **1**, 0061 (2017).
56. Garland, M., Yim, J. J. & Bogyo, M. A bright future for precision medicine: advances in fluorescent chemical probe design and their clinical application. *Cell Chem. Biol.* **23**, 122–136 (2016).
57. Lavis, L. D. & Raines, R. T. Bright ideas for chemical biology. *ACS Chem. Biol.* **3**, 142–155 (2008).
58. Liu, Z., Lavis, L. D. & Betzig, E. Imaging live-cell dynamics and structure at the single-molecule level. *Mol. Cell* **58**, 644–659 (2015).
59. Lavis, L. D. & Raines, R. T. Brightest building blocks for chemical biology. *ACS Chem. Biol.* **9**, 855–866 (2014).
60. Lavis, L. D. Chemistry is dead. Long live chemistry! *Biochemistry* **56**, 5165–5170 (2017).
61. Grimm, J. B. et al. A general method to improve fluorophores for live-cell and single-molecule microscopy. *Nat. Methods* **12**, 244–250 (2015).
62. Grimm, J. B. et al. A general method to fine-tune fluorophores for live-cell and in vivo imaging. *Nat. Methods* **14**, 987–994 (2017).
63. Butkevich, A. N., Lukinavic˘ius, G., D'Este, E. & Hell, S. W. Cell-permeant large Stokes shift dyes for transfection-free multicolor nanoscopy. *J. Am. Chem. Soc.* **139**, 12378–12381 (2017).
64. Dojindo Molecular Technologies. Cell counting kit-8: Technical Manual. *Dojindo* https://www.dojindo.com/TechnicalManual/Manual_CK04.pdf (2016).
65. Dunn, K. W., Kamocka, M. M. & McDonald, J. H. A practical guide to evaluating colocalization in biological microscopy. *Am. J. Physiol. Cell Physiol.* **300**, C723–C742 (2011).
66. Consoli, G. M. L. et al. Design and synthesis of a multivalent fluorescent folate–calix[4]arene conjugate: cancer cell penetration and intracellular localization. *Org. Biomol. Chem.* **13**, 3298–3307 (2015).
67. Consoli, G. M. L., Granata, G. & Geraci, C. Design, synthesis, and drug solubilising properties of the first folate–calix[4]arene conjugate. *Org. Biomol. Chem.* **9**, 6491–6495 (2011).
68. Zhu, M. & Yang, C. Blue fluorescent emitters: design tactics and applications in organic light-emitting diodes. *Chem. Soc. Rev.* **42**, 4963–4976 (2013).
69. Shimizu, M. & Hiyama, T. Organic fluorophores exhibiting highly efficient photoluminescence in the solid state. *Chem. Asian J.* **5**, 1516–1531 (2010).
70. Han, T.-H. et al. Extremely efficient flexible organic light-emitting diodes with modified graphene anode. *Nat. Photonics* **6**, 105–110 (2012).
71. Tanaka, T., Nishio, I., Sun, S.-T. & Ueno-Nishio, S. Collapse of gels in an electric field. *Science* **218**, 467–469 (1982).
72. Zhang, Q. M. et al. An all-organic composite actuator material with a high dielectric constant. *Nature* **419**, 284–287 (2002).
73. Asamitsu, A., Tomioka, Y., Kuwahara, H. & Tokura, Y. Current switching of resistive state in magnetoresistive manganites. *Nature* **388**, 50–52 (1997).
74. Fernandez, C. A. et al. An electrically switchable metal-organic framework. *Sci. Rep.* **4**, 6114 (2014).
75. Hasell, T., Schmidtmann, M. & Cooper, A. I. Molecular doping of porous cages. *J. Am. Chem. Soc.* **133**, 14920–14923 (2011).
76. Hertzsch, T., Budde, F., Weber, E. & Hulliger, J. Supramolecular-wire confinement of I_2 molecules in channels of the organic zeolite tris(*o*-phenylenedioxy) cyclotriphosphazene. *Angew. Chem. Int. Ed.* **41**, 2281–2284 (2002).
77. Guan, L., Suenaga, K., Shi, Z., Gu, Z. & Iijima, S. Polymorphic structures of iodine and their phase transition in confined nanospace. *Nano Lett.* **7**, 1532–1535 (2007).
78. Teitelbaum, R. C., Ruby, S. L. & Marks, T. J. On the structure of starch-iodine. *J. Am. Chem. Soc.* **100**, 3215–3217 (1978).
79. Konishi, T., Tanaka, W., Kawai, T. & Fujikawa, T. Iodine *L*-edge XAFS study of linear polyiodide chains in amylose and α-cyclodextrin. *J. Synchrotron Radiat.* **8**, 737–739 (2001).
80. Cui, Y., Yue, Y., Qian, G. & Chen, B. Luminescent functional metal–organic frameworks. *Chem. Rev.* **112**, 1126–1162 (2012).
81. Mukherjee, S. & Thilagar, P. Organic white-light emitting materials. *Dyes Pigments* **110**, 2–27 (2014).
82. Iwamoto, T., Watanabe, Y., Sadahiro, T., Haino, T. & Yamago, S. Size-selective encapsulation of C_{60} by [10]cycloparaphenylene: formation of the shortest fullerene-peapod. *Angew. Chem. Int. Ed.* **50**, 8342–8344 (2011).
83. Debije, M. G. & Verbunt, P. P. C. Thirty years of luminescent solar concentrator research: solar energy for the built environment. *Adv. Energy Mater.* **2**, 12–35 (2012).
84. Meinardi, F. et al. Large-area luminescent solar concentrators based on 'Stokes-shift-engineered' nanocrystals in a mass-polymerized PMMA matrix. *Nat. Photonics* **8**, 392–399 (2014).
85. Meinardi, F. et al. Doped halide perovskite nanocrystals for reabsorption-free luminescent solar concentrators. *ACS Energy Lett.* **2**, 2368–2377 (2017).
86. Papucci, C. et al. Green/yellow-emitting conjugated heterocyclic fluorophores for luminescent solar concentrators. *Eur. J. Org. Chem.* **2018**, 2657–2666 (2018).
87. Sol, J. A. H. P. et al. Temperature-responsive luminescent solar concentrators: tuning energy transfer in a liquid crystalline matrix. *Angew. Chem. Int. Ed.* **57**, 1030–1033 (2018).
88. Krumer, Z., van Sark, W. G. J. H. M., Schropp, R. E. I. & de Mello Donegá, C. Compensation of self-absorption losses in luminescent solar concentrators by increasing luminophore concentration. *Sol. Energy Mater. Sol. Cells* **167**, 133–139 (2017).
89. Ball, M. et al. Conjugated macrocycles in organic electronics. *Acc. Chem. Res.* **52**, 1068–1078 (2019).
90. Van Raden, J. M., Darzi, E. R., Zakharov, L. N. & Jasti, R. Synthesis and characterization of a highly strained donor–acceptor nanohoop. *Org. Biomol. Chem.* **14**, 5721–5727 (2016).
91. Hines, D., Darzi, E. R., Jasti, R. & Kamat, P. Carbon nanohoops: excited singlet and triplet behavior of aza[8]CPP and 1,15-diaza[8]CPP. *J. Phys. Chem. A* **119**, 8083–8089 (2015).
92. Darzi, E. R. et al. Synthesis, properties, and design principles of donor–acceptor nanohoops. *ACS Cent. Sci.* **1**, 335–342 (2015).
93. Kuwabara, T., Orii, J., Segawa, Y. & Itami, K. Curved oligophenylenes as donors in shape-persistent donor–acceptor macrocycles with solvatofluorochromic properties. *Angew. Chem. Int. Ed.* **54**, 9646–9649 (2015).
94. Canola, S., Graham, C., Pérez-Jiménez, A. J., Sancho-García, J. C. & Negri, F. Charge transport parameters for carbon based nanohoops and donor–acceptor derivatives. *Phys. Chem. Chem. Phys.* **21**, 2057–2068 (2019).
95. Hu, L., Guo, Y., Yan, X., Zeng, H. & Zhou, J. Electronic transport properties in [*n*]cycloparaphenylenes molecular devices. *Phys. Lett. A* **381**, 2107–2111 (2017).
96. Pérez-Guardiola, A., Pérez-Jiménez, A. J., Muccioli, L. & Sancho-García, J. C. Structure and charge transport properties of cycloparaphenylene monolayers on graphite. *Adv. Mater. Interfaces* **6**, 1801948 (2019).
97. Sancho-García, J. C., Moral, M. & Pérez-Jiménez, A. J. Effect of cyclic topology on charge-transfer properties of organic molecular semiconductors: the case of cycloparaphenylene molecules. *J. Phys. Chem. C* **120**, 9104–9111 (2016).
98. Lin, J. B., Darzi, E. R., Jasti, R., Yavuz, I. & Houk, K. N. Solid-state order and charge mobility in [5]- to [12] cycloparaphenylenes. *J. Am. Chem. Soc.* **141**, 952–960 (2019).
99. Segawa, Y. et al. Concise synthesis and crystal structure of [12]cycloparaphenylene. *Angew. Chem. Int. Ed.* **50**, 3244–3248 (2011).
100. Kayahara, E., Sakamoto, Y., Suzuki, T. & Yamago, S. Selective synthesis and crystal structure of [10] cycloparaphenylene. *Org. Lett.* **14**, 3284–3287 (2012).
101. Segawa, Y., Šenel, P., Matsuura, H., Omachi, H. & Itami, K. [9]Cycloparaphenylene: nickel-mediated synthesis and crystal structure. *Chem. Lett.* **40**, 423–425 (2011).
102. Sibbel, F., Matsui, K., Segawa, Y., Studer, A. & Itami, K. Selective synthesis of [7]- and [8]cycloparaphenylenes. *Chem. Commun.* **50**, 954–956 (2014).
103. Fukushima, T. et al. Polymorphism of [6] cycloparaphenylene for packing structure-dependent host–guest interaction. *Chem. Lett.* **46**, 855–857 (2017).
104. Yavuz, I., Lopez, S. A., Lin, J. B. & Houk, K. N. Quantitative prediction of morphology and electron transport in crystal and disordered organic semiconductors. *J. Mater. Chem. C* **4**, 11238–11243 (2016).
105. Zabula, A. V., Filatov, A. S., Xia, J., Jasti, R. & Petrukhina, M. A. Tightening of the nanobelt upon multielectron reduction. *Angew. Chem. Int. Ed.* **52**, 5033–5036 (2013).
106. Spisak, S. N., Wei, Z., Darzi, E., Jasti, R. & Petrukhina, M. A. Highly strained [6]cyclopara-phenylene: crystallization of an unsolvated polymorph and the first mono- and dianions. *Chem. Commun.* **54**, 7818–7821 (2018).
107. Golder, M. R., Wong, B. M. & Jasti, R. Photophysical and theoretical investigations of the [8]cycloparaphenylene radical cation and its charge-resonance dimer. *Chem. Sci.* **4**, 4285–4291 (2013).
108. Kayahara, E. et al. Isolation and characterization of the cycloparaphenylene radical cation and dication. *Angew. Chem. Int. Ed.* **52**, 13722–13726 (2013).
109. Toriumi, N., Muranaka, A., Kayahara, E., Yamago, S. & Uchiyama, M. In-plane aromaticity in cycloparaphenylene dications: a magnetic circular dichroism and theoretical study. *J. Am. Chem. Soc.* **137**, 82–85 (2015).

110. Kayahara, E., Kouyama, T., Kato, T. & Yamago, S. Synthesis and characterization of [*n*]CPP (*n* = 5, 6, 8, 10, and 12) radical cation and dications: size-dependent absorption, spin, and charge delocalization. *J. Am. Chem. Soc.* **138**, 338–344 (2016).
111. Masumoto, Y. et al. Near-infrared fluorescence from in-plane-aromatic cycloparaphenylene dications. *J. Phys. Chem. A* **122**, 5162–5167 (2018).
112. Meijer, E. J. et al. Solution-processed ambipolar organic field-effect transistors and inverters. *Nat. Mater.* **2**, 678–682 (2003).
113. Blom, P. W. M., de Jong, M. J. M. & Vleggaar, J. J. Electron and hole transport in poly(*p*-phenylene vinylene) devices. *Appl. Phys. Lett.* **68**, 3308–3310 (1996).
114. Lei, T., Wang, J.-Y. & Pei, J. Roles of flexible chains in organic semiconducting materials. *Chem. Mater.* **26**, 594–603 (2014).
115. Reese, C. & Bao, Z. Organic single-crystal field-effect transistors. *Mater. Today* **10**, 20–27 (2007).
116. Li, C.-Z., Yip, H.-L. & Jen, A. K.-Y. Functional fullerenes for organic photovoltaics. *J. Mater. Chem.* **22**, 4161–4177 (2012).
117. Guldi, D. M., Illescas, B. M., Atienza, C. M., Wielopolski, M. & Martín, N. Fullerene for organic electronics. *Chem. Soc. Rev.* **38**, 1587–1597 (2009).
118. Babu, S. S., Möhwald, H. & Nakanishi, T. Recent progress in morphology control of supramolecular fullerene assemblies and its applications. *Chem. Soc. Rev.* **39**, 4021–4035 (2010).
119. Smith, B. W., Monthioux, M. & Luzzi, D. E. Encapsulated C_{60} in carbon nanotubes. *Nature* **396**, 323–324 (1998).
120. Smith, B. W. & Luzzi, D. E. Formation mechanism of fullerene peapods and coaxial tubes: a path to large scale synthesis. *Chem. Phys. Lett.* **321**, 169–174 (2000).
121. Hornbaker, D. J. et al. Mapping the one-dimensional electronic states of nanotube peapod structures. *Science* **295**, 828–831 (2002).
122. Barnes, J. C. et al. Semiconducting single crystals comprising segregated arrays of complexes of C_{60}. *J. Am. Chem. Soc.* **137**, 2392–2399 (2015).
123. Iwamoto, T. et al. Size- and orientation-selective encapsulation of C_{70} by cycloparaphenylenes. *Chem. Eur. J.* **19**, 14061–14068 (2013).
124. Shinohara, H. Endohedral metallofullerenes. *Rep. Prog. Phys.* **63**, 843–892 (2000).
125. Chaur, M. N., Melin, F., Ortiz, A. L. & Echegoyen, L. Chemical, electrochemical, and structural properties of endohedral metallofullerenes. *Angew. Chem. Int. Ed.* **48**, 7514–7538 (2009).
126. Rodrígues-Fortea, A., Balch, A. L. & Poblet, J. M. Endohedral metallofullerenes: a unique host–guest association. *Chem. Soc. Rev.* **40**, 3551–3563 (2011).
127. Kimura, K. et al. Evidence for substantial interaction between Gd ion and SWNT in $(Gd@C_{82})_n$@SWCNT peapods revealed by STM studies. *Chem. Phys. Lett.* **379**, 340–344 (2003).
128. Iwamoto, T. et al. Partial charge transfer in the shortest possible metallofullerene peapod, La@C_{82}C[11]cycloparaphenylene. *Chem. Eur. J.* **20**, 14403–14409 (2014).
129. Ueno, H., Nishihara, T., Segawa, Y. & Itami, K. Cycloparaphenylene-based ionic donor–acceptor supramolecule: isolation and characterization of Li^+@C_{60}C[10]CPP. *Angew. Chem. Int. Ed.* **54**, 3707–3711 (2015).
130. Isobe, H., Hitosugi, S., Yamasaki, T. & Iizuka, R. Molecular bearings of finite carbon nanotubes and fullerenes in ensemble rolling motion. *Chem. Sci.* **4**, 1293–1297 (2013).
131. Sato, S., Yamasaki, T. & Isobe, H. Solid-state structures of peapod bearings composed of finite single-wall carbon nanotube and fullerene molecules. *Proc. Natl Acad. Sci. USA* **111**, 8374–8379 (2014).
132. Isobe, H. et al. Theoretical studies on a carbonaceous molecular bearing: association thermodynamics and dual-mode rolling dynamics. *Chem. Sci.* **6**, 2746–2753 (2015).
133. Lim, G. N., Obondi, C. O. & D'Souza, F. A high-energy charge-separated state of 1.70 eV from a high-potential donor–acceptor dyad: a catalyst for energy-demanding photochemical reactions. *Angew. Chem. Int. Ed.* **55**, 11517–11521 (2016).
134. Molina-Ontoria, A. et al. [2,2′]Paracyclophane-based π-conjugated molecular wires reveal molecular-junction behavior. *J. Am. Chem. Soc.* **133**, 2370–2373 (2011).
135. Yamamoto, M., Föhlinger, J., Petersson, J., Hammarström, L. & Imahori, H. A ruthenium complex–porphyrin–fullerene-linked molecular pentad as an integrative photosynthetic model. *Angew. Chem. Int. Ed.* **56**, 3329–3333 (2017).
136. Yu, H.-Z., Baskin, J. S. & Zewail, A. H. Ultrafast dynamics of porphyrins in the condensed phase: II. Zinc tetraphenylporphyrin. *J. Phys. Chem. A* **106**, 9845–9854 (2002).
137. Guldi, D. M. & Prato, M. Excited-state properties of C_{60} fullerene derivatives. *Acc. Chem. Res.* **33**, 695–703 (2000).
138. Omachi, H., Nakayama, T., Takahashi, E., Segawa, Y. & Itami, K. Initiation of carbon nanotube growth by well-defined carbon nanorings. *Nat. Chem.* **5**, 572–576 (2013).
139. Scott, L. T. Conjugated belts and nanorings with radially oriented p orbitals. *Angew. Chem. Int. Ed.* **42**, 4133–4135 (2003).
140. Tan, L.-L. et al. Pillar[5]arene-based SOF for highly selective CO_2-capture at ambient conditions. *Adv. Mater.* **26**, 7027–7031 (2014).
141. Lim, S. et al. Cucurbit[6]uril: organic molecular porous material with permanent porosity, exceptional stability, and acetylene sorption properties. *Angew. Chem. Int. Ed.* **47**, 3352–3355 (2008).
142. Matsuda, R. et al. Temperature responsive channel uniformity impacts on highly guest-selective adsorption in a porous coordination polymer. *Chem. Sci.* **1**, 315–321 (2010).
143. Zhang, D. et al. In situ formation of nanofibers from purpurin18-peptide conjugates and the assembly induced retention effect in tumor sites. *Adv. Mater.* **27**, 6125–6130 (2015).
144. Zheng, X. et al. Tracking cancer metastasis in vivo by using an iridium-based hypoxia-activated optical oxygen nanosensor. *Angew. Chem. Int. Ed.* **54**, 8094–8099 (2015).
145. Jiang, X. et al. Solid tumor penetration by integrin-mediated pegylated poly(trimethylene carbonate) nanoparticles loaded with paclitaxel. *Biomaterials* **34**, 1739–1746 (2013).
146. Liu, C., Zhen, X., Wang, X., Wu, W. & Jiang, X. Cellular entry fashion of hollow milk protein spheres. *Soft Matter* **7**, 11526–11534 (2011).
147. Sorkin, A. & Goh, L. K. Endocytosis and intracellular trafficking of ErbBs. *Exp. Cell Res.* **315**, 683–696 (2009).
148. Thalladi, V. R. et al. C–H · · · F interactions in the crystal structures of some fluorobenzenes. *J. Am. Chem. Soc.* **120**, 8702–8710 (1998).
149. Coates, G. W., Dunn, A. R., Henling, L. M., Dougherty, D. A. & Grubbs, R. H. Phenyl–perfluorophenyl stacking interactions: a new strategy for supermolecule construction. *Angew. Chem. Int. Ed.* **36**, 248–251 (1997).
150. Patrick, C. R. & Prosser, G. S. A molecular complex of benzene and hexafluorobenzene. *Nature* **187**, 1021 (1960).
151. Kissel, P., Murray, D. J., Wulftange, W. J., Catalano, V. J. & King, B. T. A nanoporous two-dimensional polymer by single-crystal-to-single-crystal photopolymerization. *Nat. Chem.* **6**, 774–778 (2014).
152. Salonen, L. M., Ellermann, M. & Diederich, F. Aromatic rings in chemical and biological recognition: energetics and structures. *Angew. Chem. Int. Ed.* **50**, 4808–4842 (2011).
153. Falcaro, P. et al. Centimetre-scale micropore alignment in oriented polycrystalline metal–organic framework films via heteroepitaxial growth. *Nat. Mater.* **16**, 342–348 (2017).
154. Holt, J. K. et al. Fast mass transport through sub-2-nanometer carbon nanotubes. *Science* **312**, 1034–1037 (2006).
155. Tunuguntla, R. H., Allen, F. I., Kim, K., Belliveau, A. & Noy, A. Ultrafast proton transport in sub-1-nm diameter carbon nanotube porins. *Nat. Nanotechnol.* **11**, 639–644 (2016).
156. Wang, H. et al. Selective synthesis of (9,8) single walled carbon nanotubes on cobalt incorporated TUD-1 catalysts. *J. Am. Chem. Soc.* **132**, 16747–16749 (2010).
157. Sanchez-Valencia, J. R. et al. Controlled synthesis of single-chirality carbon nanotubes. *Nature* **512**, 61–64 (2014).

Acknowledgements
The authors are grateful for support from the National Science Foundation (CHE-1800586, CHE-1808791), the Department of Energy (DE-SC0019017) and the UO OHSU Seed Grant Program.

Author contributions
Both authors contributed equally to the preparation of this manuscript.

Competing interests
The authors declare no competing interests.